

California Polytechnic State University  
San Luis Obispo, CA 93407

FINAL  
11-02-02  
0015  
30672  
105P

Numerical Design of Advanced Multi-Element Airfoils

Final Report  
October 1994

N95-15762

Unclass

G3/02 0030672

NASA Cooperative Agreement NCC-2-813

Donovan L. Mathias  
Russell M. Cummings  
Aeronautical Engineering Department

(NASA-CR-197135) NUMERICAL DESIGN  
OF ADVANCED MULTI-ELEMENT AIRFOILS  
Final Report (California  
Polytechnic State Univ.) 105 p

# NAVIER-STOKES ANALYSIS OF THE FLOW ABOUT A FLAP EDGE

Donovan L. Mathias  
Russell M. Cummings

Aeronautical Engineering Department  
California Polytechnic State University  
San Luis Obispo, CA 93407

## ABSTRACT

The current study extends the application of computational fluid dynamics to three-dimensional high-lift systems. Structured, overset grids are used in conjunction with an incompressible Navier-Stokes flow solver to investigate flow over a two-element high-lift configuration. The computations were run in a fully turbulent mode using the one-equation Baldwin-Barth turbulence model. The geometry consisted of an unswept wing which spanned a wind tunnel test section. Flows over full and half-span Fowler flap configurations were computed. Grid resolution issues were investigated in two-dimensional studies of the flapped airfoil. Results of the full-span flap wing agreed well with experimental data and verified the method. Flow over the wing with the half-span was computed to investigate the details of the flow at the free edge of the flap. The results illustrated changes in flow streamlines, separation locations, and surface pressures due to the vortex shed from the flap edge.

## TABLE OF CONTENTS

	Page
1. INTRODUCTION .....	1
1.1 MOTIVATION FOR RESEARCH .....	1
1.2 PREVIOUS WORK .....	2
1.3 SUMMARY OF THE PRESENT STUDY .....	6
2. GOVERNING EQUATIONS .....	8
2.1 INTRODUCTION .....	8
2.2 INCOMPRESSIBLE NAVIER-STOKES EQUATIONS .....	8
2.3 TRANSFORMED EQUATIONS .....	12
2.4 BALDWIN-BARTH TURBULENCE MODEL .....	19
3. NUMERICAL METHODS .....	22
3.1 INTRODUCTION .....	22
3.2 ARTIFICIAL COMPRESSIBILITY FOR STEADY STATE PROBLEMS .....	22
3.3 DIFFERENCING .....	24
3.4 IMPLICIT SCHEME .....	29
4. COMPUTATIONAL GRIDS AND BOUNDARY CONDITIONS.....	31
4.1 INTRODUCTION .....	31
4.2 GEOMETRY .....	31
4.3 GRID BUILDING PROCESS.....	32
4.4 AIRFOIL GRIDS .....	34
4.5 FULL-SPAN FLAP GRIDS.....	36
4.6 HALF-SPAN FLAP GRIDS.....	37
4.7 BOUNDARY CONDITIONS .....	39
5. RESULTS AND DISCUSSION .....	41
5.1 INTRODUCTION .....	41

5.2	TWO-DIMENSIONAL AIRFOIL RESULTS.....	41
5.3	FULL-SPAN FLAP RESULTS.....	44
5.3	HALF-SPAN FLAP RESULTS.....	46
6.	CONCLUSIONS AND RECOMMENDATIONS .....	55
	REFERENCES .....	57

## LIST OF TABLES

Table

Page

1. Flap rigging parameters..... 31

## LIST OF FIGURES

Figure	Page
1. Trends in Boeing transport high-lift system development (from Reference 3) .....	61
2. Lift efficiency versus high-lift system complexity (from Reference 4) .....	61
3. Curved computational mesh .....	62
4. Relationship between physical and computational domains .....	62
5. NACA 632-215 Mod. B airfoil .....	63
6. NACA 632-215 Mod. B airfoil with 30% chord Fowler flap in take-off configuration .....	63
7. NACA 632-215 Mod. B airfoil with 30% chord Fowler flap in landing configuration .....	64
8. Definition of gap and overlap .....	64
9. Half-span flap geometry .....	65
10. A two-dimensional grid plane .....	66
11. Overset grids before removing points inside flap surface .....	66
12. Chimera interpolation stencil .....	67
13. Use of hole-cuts to create overset grids .....	67
14. Hole-cut in a computational mesh .....	68
15. Main element wake cut placement .....	68
16. Landing configuration airfoil grid .....	69
17. Exposed surface at flapped/unflapped intersection .....	70
18. Patch grid plane	70

19. Flap edge grid plane .....	71
20. Boundary conditions at flapped/unflapped intersection .....	71
21. Half-span flap surface grid .....	72
22. Lift coefficient versus angle of attack for two-dimensional take-off configuration .....	73
23. Lift coefficient versus angle of attack for two-dimensional landing configuration .....	73
24. Pressure distribution for two-dimensional take-off configuration, $\alpha=0^\circ$ .....	74
25. Pressure distribution for two-dimensional take-off configuration, $\alpha=10^\circ$ .....	74
26. Pressure distribution for two-dimensional landing configuration, $\alpha=0^\circ$ .....	75
27. Pressure distribution for two-dimensional landing configuration, $\alpha=10^\circ$ .....	75
28. Pressure distribution for two-dimensional landing configuration without wind tunnel walls, $\alpha=0^\circ$ .....	76
29. Surface curvature for flapped main element .....	76
30. Pressure distributions for three spanwise stations on full-span flap, $\alpha=10^\circ$ .....	77
31. Pressure distributions computed with INS2D-UP and INS3D-UP for full-span flap, $\alpha=10^\circ$ .....	77
32. Experimental and computational full-span flap pressure distributions, $\alpha=10^\circ$ .....	78
33. Particle traces colored by velocity magnitude for half- span flap in landing configuration, $\alpha=10^\circ$ .....	79

34. Particle traces colored by velocity magnitude for half-span flap in take-off configuration, $\alpha=10^\circ$ .....	80
35. Lift-distribution for landing case, $\alpha=10^\circ$ .....	81
36. Lift-distribution for take-off case, $\alpha=10^\circ$ .....	81
37. Spanwise pressure variation for landing configuration unflapped main element, $\alpha=10^\circ$ .....	82
38. Spanwise pressure variation for landing configuration flapped main element, $\alpha=10^\circ$ .....	82
39. Spanwise pressure variation for landing configuration flap element, $\alpha=10^\circ$ .....	83
40. Flap surface particle traces for landing configuration.....	84
41. Pressure distribution comparison between half-span and airfoil computations for landing configuration flap element, $\alpha=10^\circ$ .....	85
42. Unflapped main element surface particle traces for landing configuration.....	86
43. Pressure distribution comparison between half-span and airfoil computations for landing configuration unflapped element, $\alpha=10^\circ$ .....	87
44. Spanwise pressure variation for landing configuration unflapped main element, $\alpha=10^\circ$ .....	87
45. Spanwise pressure variation for landing configuration flapped main element, $\alpha=10^\circ$ .....	88
46. Spanwise pressure variation for landing configuration flap element, $\alpha=10^\circ$ .....	88
47. Flap station numbering .....	89

48. Particle traces at station 1 on flap element in landing	
position .....	89
49. Particle traces at station 2 on flap element in landing	
position .....	90
50. Particle traces at station 3 on flap element in landing	
position .....	90
51. Particle traces at station 4 on flap element in landing	
position .....	91
52. Particle traces at station 5 on flap element in landing	
position .....	91
53. Particle traces at station 6 on flap element in landing	
position .....	92
54. Particle traces at station 7 on flap element in landing	
position .....	92
55. Particle traces at station 8 on flap element in landing	
position .....	93
56. Particle traces colored by pressure at the flap edge of	
landing configuration .....	94
57. Secondary recirculation regions on flap edge for	
landing configuration .....	95

# CHAPTER 1

## INTRODUCTION

### 1.1 MOTIVATION FOR RESEARCH

High-lift systems continue to be an important consideration in the design of transport aircraft. This is due to the tremendous impact they have on the performance of the aircraft. For example, when considering a large, generic, twin-engine transport a 1.5% increase in  $CL_{max}$  will increase available payload by 6600 lb. at a fixed approach speed [1]. Similarly, a 1% increase in take-off L/D will increase the payload by 2800 lb [1]. According to Butter [2], a 5% increase in landing  $CL_{max}$  is approximately worth a 25% increase in payload. These relationships illustrate how even a small increase in high-lift system performance can make a big difference in the profitability of an aircraft.

High-lift system performance is not the only issue, however. Mechanical complexity also factors into the overall evaluation of the system. The trend over the years has been to resort to added complexity to gain high-lift system performance (Figure 1 [3]). This tends to reduce the increased payload benefits illustrated previously because of the added weight and maintenance costs of the complex high-lift system. It is possible to gain performance without the added complexity, as illustrated by the Airbus aircraft in Figure 2 [4]. The Airbus aircraft (A300-A340) all show a similar  $CL_{max}$  to the Boeing aircraft (B727-747) at a lower complexity level.

A better understanding of high-lift flows is needed to continue increasing the performance of high-lift systems while decreasing their complexity. It is likely that the ability to analyze three-dimensional flows will play a key role in such an improved understanding. Butter predicts that improvements in maximum lift will come from the ability to design for high Reynolds numbers and from a better

understanding of three-dimensional flows [2]. This study addresses three-dimensional flows through the computational analysis of a simple high-lift system.

## 1.2 PREVIOUS WORK

The high potential for payoff associated with high-lift system aerodynamics has stimulated much research in this field. Almost all of the literature falls within two categories: survey papers or two-dimensional studies. This section of the thesis is dedicated to summarizing the major high-lift research to date.

The standard for survey papers in the high-lift arena was established by A. M. O. Smith's classic Wright Brothers Lecture [5]. Smith's paper started the "modern" era of high-lift system understanding. He dispelled the popular belief that the elements of a high-lift airfoil worked together by merely providing boundary layer control via the slots between elements. He was the first to illustrate the potential flow relationship between the elements of a high-lift airfoil. Since then, there have been a number of other survey type papers on the subject [1-4, 6-8]. All of these build on the findings of Smith [5] to identify areas of high-lift flows that are not fully understood. As an example, Meredith [1] summarizes some "viscous phenomena affecting high-lift system performance" as:

- Attachment line transition from laminar to turbulent
- Relaminarization of turbulent boundary layers
- Transition of boundary layers
- Viscous wake interaction
- Confluent wakes and boundary layers
- Shock/boundary layer interaction
- Separated flows

These survey papers also typically discuss the current state-of-the-art analysis techniques, generally commenting on the lack of a suitable analysis tool. A final element that is common throughout most survey papers is a summary of past high-lift research at major aircraft companies such as Boeing [6], Fokker [8], or British Aerospace [2]. In all, these papers offer a cursory description of the flow physics associated with high-lift systems, in addition to identifying problem areas and possible analysis methods.

The vast majority of the recent high-lift research has been specifically aimed at understanding two-dimensional flows, both through experimentation and computation. The experimental studies have been particularly good at demonstrating the effects the geometry, Mach, and Reynolds numbers have on the airfoil lift and drag. Valarezo et al. has published a number of experimental investigations of three-element airfoils. His papers have been dedicated to slat and flap positioning [9,10] as well as some work on flow scale effects [11]. Valarezo's work has demonstrated adverse Reynolds number effects for multi-element airfoils, where the airfoil  $C_{l_{max}}$  decreases as the Reynolds number increase. Chin et al. has provided some of the most detailed high-lift flow measurements in his measurements of the flow over a three-element airfoil [12]. This work has proved extremely useful to CFD code validation. An innovative, high-lift concept was investigated by Ross, Storms, and Carrannanto [13] and Storms and Ross [14] in their investigation of lift enhancing tabs on multi-element airfoils. Their preliminary findings suggest that in some cases  $C_{l_{max}}$  can be improved with the addition of simple tabs near the trailing edge of an airfoil.

There have been literally hundreds of attempts to analyze high-lift systems using coupled inviscid/viscous methods-the few mentioned in this thesis are representative of most of this work. Most of the research used a two-dimensional potential method with an integral boundary layer scheme [15-17]. The primary

advantage of this approach is the relatively low computational requirements. This makes these methods very attractive to designers who perform many iterations in the design process. More recently, quasi-three-dimensional versions of inviscid/viscous methods have been introduced [18]. This method combines a three-dimensional lifting surface method with two-dimensional viscous modeling to compute high-lift flows. The limit to this approach lies in the fact that the complex, three-dimensional viscous effects are represented with simple two-dimensional models. Also, with the three-dimensional potential code the computational requirements increase significantly. One of the more successful inviscid/viscous approaches is the MSES code [19]. MSES solves the two-dimensional Euler equations simultaneously with integral boundary layer equations. This method has given very good results, but is again limited to two dimensions.

With the recent availability of quality experimental data, a great deal of CFD code validation work on multi-element airfoils has been performed. Due to the inherently viscous nature of the high-lift flowfield, most of the recent numerical investigations have solved some form of the Navier-Stokes equations. Perhaps the most widely used approach involves the solution of the incompressible Navier-Stokes equations on structured, Chimera grids [20-23]. Others have utilized the flexibility of the Chimera grid scheme to solve compressible, full [24] or thin-layer [25, 26] Navier-Stokes equations. Recently, some investigators have successfully solved Euler [27] and compressible Navier-Stokes equations on unstructured meshes [28]. All of the Navier-Stokes solutions mentioned here have demonstrated some ability to accurately resolve high-lift flows. The vast majority of the two-dimensional computational research discussed here was dedicated to analysis of conventional high-lift airfoils. A notable exception to this is Carrannanto et al.'s analysis of the lift-enhancing tab concept [23] experimentally investigated by Ross, Storms, and Carrannanto and Storms and Ross [13, 14].

There are a few papers that do not fit neatly into one of the above categories, such as the papers that focus on specific flow features. For example, Savory et al. [29] discusses flow physics in the gaps between elements of a high-lift system, Horton [30] dedicates his paper to the physics of high-lift flow separation, and van Dam et al. [31] discusses boundary layer transition and relaminarization on high-lift wings. Descriptions of the respective phenomena are included along with speculations about the driving mechanisms. As the understanding of high-lift flows increases, more of this type of research is sure to appear. Another paper topic is based on the development or assessment of high-lift system analysis techniques [32]. In a different type of paper, a summary of high-lift system design at Deutsche-Airbus is given by Flaig and Hilbig [4].

The lack of three-dimensional research becomes obvious when surveying the literature. This is made even more surprising by the fact that most of the survey papers discussed above indicate three-dimensional flow effects as a major driving force in high-lift system performance. Many of the survey papers contain some three-dimensional test results, but these offer only integrated effects without the details needed to begin to analyze the flow physics. On the computational side of things, very little has been done in the way of modeling three-dimensional high-lift systems. Most recently, Rogers [21] performed a preliminary Navier-Stokes analysis of a T-39 Sabreliner wing equipped with a high-lift system. Studies that computationally investigated complete aircraft with flaps deployed have lacked the grid resolution to adequately resolve the flow about the high-lift systems. They do, however, offer hope that a high-lift flowfield could be analyzed computationally with the proper grid resolution.

### 1.3 SUMMARY OF THE PRESENT STUDY

A CFD approach was chosen for this study because it may provide detailed flow information. Due to the viscous nature of high-lift flows, the simplest governing equations that could be used were the incompressible Navier-Stokes equations. It has been shown that compressibility can become an issue in high-lift flows for freestream Mach numbers as low as 0.15 [7], but for this study an incompressible solver was used due to the large savings of computer time. For high-lift flows at lower Mach numbers ( $M_\infty \leq 0.2$ ), any appearance of compressibility usually occurs in the vicinity of the slat element. The configurations investigated here were all two-element wing sections without slats. Therefore, it was felt that any loss of accuracy involved with assuming incompressible flow would be kept to a minimum.

The goal of this study was to apply current computational tools to a simple, three-dimensional high-lift system. The work began with a two-dimensional computational study of the flapped airfoil that represented the basic geometry for the entire study. The two-dimensional work allowed for a grid resolution study and established a baseline set of results with which to compare at later stages in the investigation. The first three-dimensional computations were performed for a wing that fully spanned the test section of a wind tunnel. This was essentially the same configuration as the airfoils studied in two dimension, except the three-dimensional flow solver was used. These results were compared to the two-dimensional computations and experimental data to validate the approach. The major focus of the research was the computation of the flow over a wing with a half-span flap. A grid scheme was developed to adequately resolve this flow, so the details of the flow physics could be investigated.

This project accompanies a wind tunnel test of the same geometry scheduled to occur in the NASA Ames Research Center 7-by-10 Foot Wind Tunnel. The CFD

was done prior to the experiment so that the computed results could be considered when selecting a run schedule and locating the pressure sensors on the model. Every attempt is made to match the experimental set-up in the computations so that a meaningful comparison of the results can be made. This includes matching the flow conditions and geometries as closely as possible. For this reason, the wind tunnel walls were modeled in all of the computations. False walls will be needed in the experiment to shield instrumentation and mounting hardware from the flow, effectively reducing the size of the test section to 5x10 feet [14]. This 5x10 foot test section is the one modeled in the computations. The reference chord of the physical wind tunnel model (unflapped section) is 2.5 feet. The flow at the test section of the tunnel is at a freestream Mach number of  $M_\infty = 0.2$  and a Reynolds number, based on the unflapped chord, of  $Re_c = 3.7 \times 10^6$ . All length dimensions in the computations are non-dimensionalized by the model chord.

This thesis contains a description of the geometry, governing equations, flow solver, turbulence model, and boundary conditions used for this study. The grid strategy developed to resolve flow about a three-dimensional high-lift system in an efficient manner is discussed. Computations of flow over a two-element wing between wind tunnel walls are compared with experimental results to verify the computational approach. The results for a half-span flap wing are also presented. Conclusions about the computational approach and flow physics are made.

## CHAPTER 2

### GOVERNING EQUATIONS

#### 2.1 INTRODUCTION

This chapter covers the theoretical aspects of the research. The governing flow equations and related assumptions are discussed in Section 2.2. The complete derivations are left out of this chapter and can be found in Reference [33]. Section 2.3 is dedicated to a non-dimensionalization and transformation of the governing equations which make the equations easier to solve numerically. A description of the Baldwin-Barth turbulence model makes up the final section of this chapter.

#### 2.2 INCOMPRESSIBLE NAVIER-STOKES EQUATIONS

This study involved solving the three-dimensional, incompressible Navier-Stokes (INS) equations. These equations make up a set of four partial differential equations which are derived from the laws of conservation of mass and momentum. In tensor form, the equations can be written as follows:

$$\begin{aligned}\frac{\partial u_i}{\partial x_i} &= 0 \\ \frac{\partial u_i}{\partial t} + \frac{\partial(u_i u_j)}{\partial x_j} &= -\frac{\delta_{ij}}{\rho} \frac{\partial p}{\partial x_i} + \nu \left( \frac{\partial^2 u_i}{\partial x_j^2} + \frac{\partial^2 u_j}{\partial x_i^2} \right)\end{aligned}\tag{1}$$

where  $i, j = 1, 2, 3$ . The parameters in Equation (1) are defined as follows:

$x_i$  represents the three Cartesian coordinates  $(x, y, z)$ ,

$u_i$  represents the velocity components  $(u, v, w)$ ,

$p$  is the flow static pressure,

$t$  is time,

$\rho$  is the flow density,

$\nu$  is the kinematic molecular viscosity of the fluid, and

$\delta_{ij}$  is the Kronecker delta function.

As shown, Equation (1) is classified as a mixed elliptic-parabolic set of equations [34].

The INS equations were selected because they are the simplest set of equations that could govern a high-lift flowfield. With the possible existence of flow features such as flow separation, viscous wake interaction, and confluent wakes and boundary layers, viscosity must be included in the modeling of the flow. Simpler forms of the Navier-Stokes equations (i.e. thin-layer or boundary layer equations) neglect aspects of the flow that were important to this study. It is not as obvious, however, whether the compressible or incompressible form of the Navier-Stokes equations should be used. It has been shown that compressible effects can appear in high-lift flows for freestream Mach numbers as low as  $M_\infty = 0.15$  [7]. The compressibility appearing at such low Mach numbers is usually restricted to the slat element because the flow velocities are highest in this region. The simple geometry investigated in this study contains only main wing and flap elements, therefore reducing the possible effects of compressibility. Because the incompressible equations have been successfully applied to high-lift flows in two dimensions [20-23], it was decided that any loss in accuracy due to the choice of governing equations was minor when compared to the computational efficiency gained by using an incompressible flow solver.

In general, there exists no closed form solution to the incompressible Navier-Stokes equations. Therefore, numerical methods are required to obtain a solution. A finite difference approach is used in this study. Finite difference methods replace the flowfield with a finite number of points (grid points) and solve the equations at these points. The primary concern with this method is that the equations will only

resolve flow phenomena that have characteristic scales greater than the distance between grid points. For laminar flows, this is not a problem because the smallest scales are on the order of the boundary layer thickness. For turbulent flows, the problem becomes much more difficult. The smallest scales in turbulent flows, the Kolmogorov microscales, are far too small to be resolved with grid points for all but the simplest flows [34]. Not only would points be needed to resolve these scales in the boundary layer, as with the laminar case, but this resolution would be required at every place in the flow containing turbulence. There is disagreement about the exact spacing required to resolve turbulent flow features, but one estimate is that  $10^5$  grid points would be required to resolve  $1 \text{ cm}^3$  of a typical flow field [34]. Clearly this is not currently feasible for most practical aeronautical applications. Therefore, additional assumptions are needed.

One way to overcome this difficulty is to assume that physical flow properties consist of two components, one component associated with the mean flow property and the other associated with a turbulent fluctuation. For example, the velocity would be expressed as

$$u = \bar{u} + u' \quad (2)$$

where  $u$  is the total velocity,  $\bar{u}$  is the mean velocity, and  $u'$  is the unsteady turbulent velocity fluctuation. All of the parameters in Equation (1) are replaced with this representation, and the entire equation is time averaged. The resultant set of equations are the well known Reynolds Averaged Navier-Stokes (RANS) equations [34]:

$$\frac{\partial \bar{u}_i}{\partial x_i} = 0 \quad (3)$$

$$\frac{\partial \bar{u}_i}{\partial t} + \frac{\partial (\bar{u}_i \bar{u}_j)}{\partial x_j} = -\frac{\delta_{ij}}{\rho} \frac{\partial \bar{p}}{\partial x_i} + \frac{1}{\rho} (\bar{\tau}_{ij} - \rho \overline{u'_i u'_j})$$

where  $\tau_{ij} = \mu \left( \frac{\partial \bar{u}_i}{\partial x_j} + \frac{\partial \bar{u}_j}{\partial x_i} \right)$  and  $\mu = \frac{\nu}{\rho}$ .

A note concerning this time averaging is in order. The time over which to average the equations is chosen to be large enough to capture small scale turbulent effects but small enough not to average out large scale unsteadiness in the flow. In practice, this is not a problem because the small turbulent time scales are much shorter than those associated with the flow in general. From examination of Equation (3) it is seen that Reynolds averaging process changes the equations in two ways. First, all the parameters in Equation (1) are replaced with an averaged value indicated by the overbar. The second difference is the addition of an extra term  $(-\rho \overline{u'_i u'_j})$  in Equation (3) known as the Reynolds stress. This term is "stress-like" because it adds "viscosity" to the flow due to turbulent fluctuations. The Boussinesq approximation uses this stress-like behavior to form the following approximation of the Reynolds stress based on the laminar stress relation:

$$-\rho \overline{u'_i u'_j} = \nu_t \left( \frac{\partial \bar{u}_i}{\partial x_j} + \frac{\partial \bar{u}_j}{\partial x_i} \right) \quad (4)$$

where  $\nu_t$  represents the turbulent, or eddy, viscosity. When Equation (4) is substituted into Equation (3), the following relationship is obtained:

$$\frac{\partial \bar{u}_i}{\partial t} + \frac{\partial (\bar{u}_i \bar{u}_j)}{\partial x_j} = -\frac{\delta_{ij}}{\rho} \frac{\partial \bar{p}}{\partial x_i} + (\nu + \nu_t) \left( \frac{\partial \bar{u}_i}{\partial x_j} + \frac{\partial \bar{u}_j}{\partial x_i} \right) \quad (5)$$

In Equation (5) all of the effects of flow turbulence are modeled by a term,  $\nu_t$ , that acts like additional molecular viscosity. But  $\nu_t$  is an additional unknown, requiring

an additional equation, known as a turbulence model, to make the set determinate once again. This is known as the closure problem. The turbulence model is discussed in Section 2.4. All of the equations hereafter are assumed to be time averaged unless specifically stated otherwise, and the overbars will be omitted for convenience.

### 2.3 TRANSFORMED EQUATIONS

The Reynolds Averaged Navier-Stokes equations as presented in Equation (5) are in a form that can be solved using numerical techniques. In this form, though, flows over general bodies would be very difficult to obtain because the current coordinate system would be inconvenient for a practical CFD problem. There is a non-dimensionalization and a transformation that will greatly simplify the solution of the RANS equations for complex configurations. First, the equations will be non-dimensionalized, and second they will be transformed into a generalized set of curvilinear coordinates.

Many possibilities exist for non-dimensionalizing the RANS equations. The approach presented here is based on the implementation in the INS3D-UP code [35]. The following expressions are substituted into Equation (5)

$$\begin{aligned}\bar{u}_i &= \frac{u_i}{u_{ref}}, \quad \bar{x}_i = \frac{x_i}{x_{ref}}, \quad \bar{t} = \frac{tu_{ref}}{x_{ref}}, \quad \bar{p} = \frac{p - p_{ref}}{\rho u_{ref}^2}, \\ \bar{\tau}_{ij} &= \frac{\tau_{ij}}{\rho u_{ref}^2}, \quad \bar{v} = \frac{v}{x_{ref} u_{ref}} = Re^{-1}\end{aligned}\tag{6}$$

which give

$$\begin{aligned}\frac{\partial \bar{u}_i}{\partial \bar{x}_i} &= 0 \\ \frac{\partial \bar{u}_i}{\partial \bar{t}} + \frac{\partial(\bar{u}_i \bar{u}_j)}{\partial \bar{x}_j} &= -\frac{\delta_{ij}}{\bar{\rho}} \frac{\partial \bar{p}}{\partial \bar{x}_i} + (\bar{v} + \bar{v}_i) \left( \frac{\partial \bar{u}_i}{\partial \bar{x}_j} + \frac{\partial \bar{u}_j}{\partial \bar{x}_i} \right)\end{aligned}\tag{7}$$

As with the time average notation, the tildes will be dropped hereafter, but the variables remain non-dimensionalized unless otherwise stated. As shown, the non-dimensionalization does not change the form of the equations, but does allow for more convenient scaling between problems.

A particularly useful form of the equations can be reached by combining Equation (13) and Equation (14) along with some rearrangement.

$$\frac{\partial U}{\partial t} + \frac{\partial E}{\partial x} + \frac{\partial F}{\partial y} + \frac{\partial G}{\partial z} = 0 \quad (8)$$

where

$$U = \begin{bmatrix} 0 \\ u \\ v \\ w \end{bmatrix}, \quad (9)$$

$$E = e - e_v, \quad F = f - f_v, \quad G = g - g_v,$$

$$e = \begin{bmatrix} u \\ u^2 + p \\ uv \\ uw \end{bmatrix}, \quad f = \begin{bmatrix} v \\ uv \\ v^2 + p \\ vw \end{bmatrix}, \quad g = \begin{bmatrix} w \\ uw \\ vw \\ w^2 + p \end{bmatrix},$$

$$e_v = \begin{bmatrix} 0 \\ \tau_{xx} \\ \tau_{xy} \\ \tau_{xz} \end{bmatrix}, \quad f_v = \begin{bmatrix} 0 \\ \tau_{yx} \\ \tau_{yy} \\ \tau_{yz} \end{bmatrix}, \quad g_v = \begin{bmatrix} 0 \\ \tau_{zx} \\ \tau_{zy} \\ \tau_{zz} \end{bmatrix}$$

where  $e, f, g$  are convective flux vectors and  $e_v, f_v, g_v$  are the viscous flux vectors. This form of the equations is known as conservation law form. Four equations have been combined into a single vector equation making its use easier from the standpoint of derivation and implementation.

Because the RANS equations, Equation (8), are to be solved using finite difference techniques, the computational mesh has a significant influence on the solution scheme. For example, if the flow problem is discretized with a mesh that is homogeneous (equal grid spacing in all directions) the finite difference schemes simplify dramatically. However, the number of physical problems that lend themselves to this type of representation are limited. Most applied flow problems require meshes which are quite curved as shown in Figure 3. The complexity of finite differences increases so significantly with an irregular mesh that most flow solvers transform the curved mesh into a homogeneous one. The flow equations are transformed and solved on the new mesh in the computational domain, and the solution is inverse transformed to yield results in the physical domain. This transformation certainly complicates the solution scheme, but the increase in complexity is less of a penalty than solving the equations on an irregular mesh. The real difficulty comes from the fact that every mesh must be conformed to suit its particular problem eliminating the possibility of an analytic expression for the general transformation. Therefore a general transformation is assumed and evaluated numerically during the solution process.

For a three dimensional flow, a transformation of the form

$$\begin{aligned}\xi &= \xi(x,y,z), \\ \eta &= \eta(x,y,z), \\ \zeta &= \zeta(x,y,z)\end{aligned}\tag{10}$$

can be assumed. In this case,  $\xi$ ,  $\eta$ , and  $\zeta$  represent orthogonal axes in the computational domain. Also, the mesh is assumed not to vary with respect to time. A two dimensional relation between the computational and physical planes is illustrated in Figure 4. Before the equations can be applied to the computational

space they must be expressed as functions of the new space variables. To do this, consider the chain rule

$$\begin{aligned}\frac{\partial}{\partial x} &= \xi_x \frac{\partial}{\partial \xi} + \eta_x \frac{\partial}{\partial \eta} + \zeta_x \frac{\partial}{\partial \zeta}, \\ \frac{\partial}{\partial y} &= \xi_y \frac{\partial}{\partial \xi} + \eta_y \frac{\partial}{\partial \eta} + \zeta_y \frac{\partial}{\partial \zeta}, \\ \frac{\partial}{\partial z} &= \xi_z \frac{\partial}{\partial \xi} + \eta_z \frac{\partial}{\partial \eta} + \zeta_z \frac{\partial}{\partial \zeta}\end{aligned}\tag{11}$$

where abbreviated partial derivative notation is used ( $\xi_x \equiv \frac{\partial \xi}{\partial x}$ , etc.). Equation (11) can be substituted into the RANS equations to transform them into computational space. Before the real usefulness of the transformation can be appreciated, a little more needs to be said concerning the metrics of the transformation ( $\xi_x, \eta_y$ , etc.). Expressions for the metrics are needed in order to evaluate transformation. To derive expressions for the metrics, consider the following differential expressions [34]:

$$\begin{aligned}dx &= x_\xi d\xi + x_\eta d\eta + x_\zeta d\zeta, \\ dy &= y_\xi d\xi + y_\eta d\eta + y_\zeta d\zeta, \\ dz &= z_\xi d\xi + z_\eta d\eta + z_\zeta d\zeta\end{aligned}\tag{12}$$

and similarly

$$\begin{aligned}d\xi &= \xi_x dx + \xi_y dy + \xi_z dz, \\ d\eta &= \eta_x dx + \eta_y dy + \eta_z dz, \\ d\zeta &= \zeta_x dx + \zeta_y dy + \zeta_z dz\end{aligned}\tag{13}$$

which can be put in the matrix form

$$\begin{aligned} A &= BC, \\ C &= DA \end{aligned} \tag{14}$$

if A, B, C, D are defined as follows:

$$\begin{aligned} A &= \begin{bmatrix} dx \\ dy \\ dz \end{bmatrix}, & B &= \begin{bmatrix} x_{\xi} & x_{\eta} & x_{\zeta} \\ y_{\xi} & y_{\eta} & y_{\zeta} \\ z_{\xi} & z_{\eta} & z_{\zeta} \end{bmatrix}, \\ C &= \begin{bmatrix} d\xi \\ d\eta \\ d\zeta \end{bmatrix}, & D &= \begin{bmatrix} \xi_x & \xi_y & \xi_z \\ \eta_x & \eta_y & \eta_z \\ \zeta_x & \zeta_y & \zeta_z \end{bmatrix} \end{aligned} \tag{15}$$

It follows that

$$B^{-1}A = B^{-1}BC = C \tag{16}$$

and since

$$C = DA \tag{14}$$

the result

$$B^{-1} = D \tag{17}$$

is attained. If B is inverted, expressions for the metrics are attained [34].

$$D = B^{-1} = J \begin{bmatrix} y_{\eta} z_{\xi} - y_{\xi} z_{\eta} & -(x_{\eta} z_{\xi} - x_{\xi} z_{\eta}) & x_{\eta} y_{\xi} - x_{\xi} y_{\eta} \\ -(y_{\xi} z_{\xi} - y_{\xi} z_{\xi}) & x_{\xi} z_{\xi} - x_{\xi} z_{\xi} & -(x_{\xi} y_{\xi} - x_{\xi} y_{\xi}) \\ y_{\xi} z_{\eta} - y_{\eta} z_{\xi} & -(x_{\xi} z_{\eta} - x_{\eta} z_{\xi}) & x_{\xi} y_{\eta} - x_{\eta} y_{\xi} \end{bmatrix} \quad (18)$$

J is the Jacobian of the transformation given by

$$J = \frac{\partial(\xi, \eta, \zeta)}{\partial(x, y, z)} = 1 / \frac{\partial(x, y, z)}{\partial(\xi, \eta, \zeta)} = 1 / \begin{vmatrix} x_{\xi} & x_{\eta} & x_{\zeta} \\ y_{\xi} & y_{\eta} & y_{\zeta} \\ z_{\xi} & z_{\eta} & z_{\zeta} \end{vmatrix} \quad (19)$$

Obviously, the determinant in Equation (19) must be non-zero for the transformation to exist. Physically, this prevents the mapping of a zero or negative cell volume in one domain to a positive cell volume in the other. The individual metrics in Equation (15) can be solved if the expressions in Equation (18), or more specifically the partial derivatives  $x_{\xi}, y_{\eta}, z_{\zeta}$ , etc., are known. There are two ways of finding values for the partial derivatives. They can be computed analytically if a closed form transformation (or inverse transformation in this case) exists. In general, however, this relationship does not exist. The alternative method requires the use of finite differences to evaluate the derivatives. The finite difference approach is used here and is discussed in the section on differencing (Section 2.4.2). For the rest of this section it is assumed that all of the metrics are known. With known metrics, Equation (8) can be transformed by using Equations (29-31).

$$\begin{aligned} & \frac{\partial U}{\partial t} + \xi_x \frac{\partial E}{\partial \xi} + \eta_x \frac{\partial E}{\partial \eta} + \zeta_x \frac{\partial E}{\partial \zeta} + \xi_y \frac{\partial F}{\partial \xi} \\ & + \eta_y \frac{\partial F}{\partial \eta} + \zeta_y \frac{\partial F}{\partial \zeta} + \xi_z \frac{\partial G}{\partial \xi} + \eta_z \frac{\partial G}{\partial \eta} + \zeta_z \frac{\partial G}{\partial \zeta} = 0 \end{aligned} \quad (20)$$

This equation can be put back into conservation law form by employing the following definitions [36]:

$$\begin{aligned} U_1 &= \frac{U}{J}, \\ E_1 &= \frac{1}{J}(E\xi_x + F\xi_y + G\xi_z), \\ F_1 &= \frac{1}{J}(E\eta_x + F\eta_y + G\eta_z), \\ G_1 &= \frac{1}{J}(E\zeta_x + F\zeta_y + G\zeta_z) \end{aligned} \quad (21)$$

Equation (20) becomes

$$\frac{\partial U_1}{\partial t} + \frac{\partial E_1}{\partial \xi} + \frac{\partial F_1}{\partial \eta} + \frac{\partial G_1}{\partial \zeta} = 0 \quad (22)$$

Recall that the vectors  $E$ ,  $F$ , and  $G$  were made up of a convective flux and a viscous flux. The viscous terms contain partial derivatives that must also be transformed using Equation (11). The transformation of the viscous fluxes is omitted here but the details can be found in Rogers [35]. The following is a summary of the results:

$$\begin{aligned} U_1 &= \frac{1}{J} \begin{bmatrix} 0 \\ u \\ v \\ w \end{bmatrix}, \quad E_1 = \frac{e_1 - e_{v1}}{J}, \quad F_1 = \frac{f_1 - f_{v1}}{J}, \quad G_1 = \frac{g_1 - g_{v1}}{J} \\ e_1 &= \begin{bmatrix} \xi_x u + \xi_y v + \xi_z w \\ \xi_x(p + u^2) + \xi_y uv + \xi_z uw \\ \xi_x uv + \xi_y(p + v^2) + \xi_z vw \\ \xi_x uw + \xi_y vw + \xi_z(p + w^2) \end{bmatrix}, \quad e_{v1} = \begin{bmatrix} 0 \\ \xi_x \tau_{xx} + \xi_y \tau_{xy} + \xi_z \tau_{xz} \\ \xi_x \tau_{xy} + \xi_y \tau_{yy} + \xi_z \tau_{yz} \\ \xi_x \tau_{xz} + \xi_y \tau_{yz} + \xi_z \tau_{zz} \end{bmatrix} \end{aligned} \quad (23)$$

$$\begin{aligned}
f_1 &= \begin{bmatrix} \eta_x u + \eta_y v + \eta_z w \\ \eta_x(p + u^2) + \eta_y uv + \eta_z uw \\ \eta_x uv + \eta_y(p + v^2) + \eta_z vw \\ \eta_x uw + \eta_y vw + \eta_z(p + w^2) \end{bmatrix}, & f_{v1} &= \begin{bmatrix} 0 \\ \eta_x \tau_{xx} + \eta_y \tau_{xy} + \eta_z \tau_{xz} \\ \eta_x \tau_{xy} + \eta_y \tau_{yy} + \eta_z \tau_{yz} \\ \eta_x \tau_{xz} + \eta_y \tau_{yz} + \eta_z \tau_{zz} \end{bmatrix}, \\
g_1 &= \begin{bmatrix} \xi_x u + \xi_y v + \xi_z w \\ \xi_x(p + u^2) + \xi_y uv + \xi_z uw \\ \xi_x uv + \xi_y(p + v^2) + \xi_z vw \\ \xi_x uw + \xi_y vw + \xi_z(p + w^2) \end{bmatrix}, & g_{v1} &= \begin{bmatrix} 0 \\ \xi_x \tau_{xx} + \xi_y \tau_{xy} + \xi_z \tau_{xz} \\ \xi_x \tau_{xy} + \xi_y \tau_{yy} + \xi_z \tau_{yz} \\ \xi_x \tau_{xz} + \xi_y \tau_{yz} + \xi_z \tau_{zz} \end{bmatrix}, \\
\tau_{xx} &= 2\nu(\xi_x \frac{\partial u}{\partial \xi} + \eta_x \frac{\partial u}{\partial \eta} + \zeta_x \frac{\partial u}{\partial \zeta}), \\
\tau_{yy} &= 2\nu(\xi_y \frac{\partial v}{\partial \xi} + \eta_y \frac{\partial v}{\partial \eta} + \zeta_y \frac{\partial v}{\partial \zeta}), \\
\tau_{zz} &= 2\nu(\xi_z \frac{\partial w}{\partial \xi} + \eta_z \frac{\partial w}{\partial \eta} + \zeta_z \frac{\partial w}{\partial \zeta}), \\
\tau_{xz} &= \nu[(\xi_x \frac{\partial u}{\partial \xi} + \eta_x \frac{\partial u}{\partial \eta} + \zeta_x \frac{\partial u}{\partial \zeta}) + (\xi_z \frac{\partial w}{\partial \xi} + \eta_z \frac{\partial w}{\partial \eta} + \zeta_z \frac{\partial w}{\partial \zeta})], \\
\tau_{xy} &= \nu[(\xi_x \frac{\partial u}{\partial \xi} + \eta_x \frac{\partial u}{\partial \eta} + \zeta_x \frac{\partial u}{\partial \zeta}) + (\xi_y \frac{\partial v}{\partial \xi} + \eta_y \frac{\partial v}{\partial \eta} + \zeta_y \frac{\partial v}{\partial \zeta})], \\
\tau_{yz} &= \nu[(\xi_y \frac{\partial v}{\partial \xi} + \eta_y \frac{\partial v}{\partial \eta} + \zeta_y \frac{\partial v}{\partial \zeta}) + (\xi_z \frac{\partial w}{\partial \xi} + \eta_z \frac{\partial w}{\partial \eta} + \zeta_z \frac{\partial w}{\partial \zeta})]
\end{aligned}$$

## 2.4 BALDWIN-BARTH TURBULENCE MODEL

The one-equation Baldwin-Barth turbulence model [37] was used for all of the cases discussed in this thesis. A number of researchers [22-24] have shown that this model does a reasonable job in predicting high-lift, multi-element airfoil flows. Specifically, Mani and Bush [24] have demonstrated a dramatic improvement in results computed with this model versus those performed using the algebraic Baldwin-Lomax model [38]. Rogers et al. recently studied four one- and two-equation models for use in computing multi-element airfoil flows [22]. He concluded that the all of the models tested "produced very similar results in most cases." This model requires approximately the same grid resolution as the algebraic models, which is significantly less than the multi-equation models require [37].

These facts, along with the relatively low computational requirements, made this model very attractive for the use in this study.

The current implementation of turbulence models in INS3D-UP requires that the code be run in a fully laminar or fully turbulent mode. All of the current cases were run in a fully turbulent mode, with no modeling of transition. This did not hurt the comparison with the experimental data too badly because transition strips were placed on the upper ( $x/c = .10$ ) and lower ( $x/c = 0.05$ ) surfaces of the main element in the experiments. No transition strips were used on the flap, but the large adverse pressure gradients typically seen on the upper surface of the flap near the leading edge are likely to cause natural transition close to the leading edge. Laminar flow is more apt to exist on the lower surface of the flap which would create an inconsistency between the computations and the experiment. This difference should have a minor effect on the flowfield as a whole. Transition strips will be used in the planned half-span flap experiment.

The Baldwin-Barth model was developed through a simplification of the standard  $k - \varepsilon$  model equations [39]. The  $k - \varepsilon$  model is a system of two partial differential equations for  $k$ , the turbulent kinetic energy production, and  $\varepsilon$ , the energy dissipation rate. To combine the  $k - \varepsilon$  equations, a new parameter,  $R_T$ , is defined that includes the turbulent kinetic energy production and dissipation terms,

$$R_T = \frac{k^2}{\nu \varepsilon} \quad (24)$$

where  $R_T$  is known as the turbulent Reynolds number. With this definition, the two partial differential equations were reduced to a single partial differential equation for  $R_T$ . The equation is iteratively solved for the entire flowfield using a line relaxation scheme. Once  $R_T$  is known, the eddy viscosity,  $\nu_t$ , can be computed from

$$v_t = C(vR_T)D_1D_2. \quad (25)$$

$$D_1 = 1 - \exp(-y^+ / A^+)$$

$$D_2 = 1 - \exp(-y^+ / A_2^+)$$

$$y^+ = u_\tau y / \nu$$

where  $u_\tau$  is the friction velocity  $\sqrt{\tau_{wall} / \rho_{wall}}$ ,  $C = 0.09$ ,  $A^+ = 26$ , and  $A_2^+ = 10$ .  $C$ ,  $A^+$ , and  $A_2^+$  are empirically determined constants [37].

## CHAPTER 3

### NUMERICAL METHODS

#### 3.1 INTRODUCTION

All of the computed results in this study were attained using the INS2D-UP and INS3D-UP (Incompressible Navier-Stokes with Upwind Differencing) flow solvers [35]. The INS codes provide a means for solving the Incompressible Navier-Stokes equations in a manner that is fast, robust, and easy to perform. This section is dedicated to describing the numerical solution scheme incorporated in INS2D-UP and INS3D-UP. The three-dimensional method is discussed because the two-dimensional method is a subset of this case. Only the aspects of the code pertinent to this research are discussed.

#### 3.2 ARTIFICIAL COMPRESSIBILITY FOR STEADY-STATE PROBLEMS

INS3D-UP solves the Incompressible RANS equations in their primitive variable form. To enhance convergence, the method of artificial compressibility is employed [40]. This method simulates a compressible flowfield by introducing artificial pressure waves which propagate through space. The implementation of this method involves adding an artificial compressibility term to the continuity equation.

$$\frac{\partial p}{\partial t} = -\beta \nabla \cdot V \quad (26)$$

In this case,  $\beta$  represents the speed at which the pressure waves travel. It is stressed that this is not a physical phenomena, but merely a numerical scheme used to enhance convergence. This relationship does not affect the final solution because the

pressure waves ( $\frac{\partial p}{\partial t}$ ) disappear as the solution approaches steady state. As a result, the steady continuity equation remains unchanged. For a steady solution, the time variable  $t$  does not represent physical time, so it can be replaced with a pseudo time term  $\tau$  [35]. This is done to avoid confusion in cases where a time-accurate solution is needed. With the addition of (26) to the terms in the RANS equations (22) become

$$\frac{\partial U_1}{\partial \tau} + \frac{\partial E_1}{\partial \xi} + \frac{\partial F_1}{\partial \eta} + \frac{\partial G_1}{\partial \zeta} = 0, \quad (27)$$

$$U_1 = \frac{1}{J} \begin{bmatrix} p \\ u \\ v \\ w \end{bmatrix}, \quad E_1 = \frac{e_1 - e_{v1}}{J}, \quad F_1 = \frac{f_1 - f_{v1}}{J}, \quad G_1 = \frac{g_1 - g_{v1}}{J},$$

$$e_1 = \begin{bmatrix} \beta(\xi_x u + \xi_y v + \xi_z w) \\ \xi_x(p + u^2) + \xi_y uv + \xi_z uw \\ \xi_x uv + \xi_y(p + v^2) + \xi_z vw \\ \xi_x uw + \xi_y vw + \xi_z(p + w^2) \end{bmatrix}, \quad e_{v1} = \begin{bmatrix} 0 \\ \xi_x \tau_{xx} + \xi_y \tau_{xy} + \xi_z \tau_{xz} \\ \xi_x \tau_{xy} + \xi_y \tau_{yy} + \xi_z \tau_{yz} \\ \xi_x \tau_{xz} + \xi_y \tau_{yz} + \xi_z \tau_{zz} \end{bmatrix},$$

$$f_1 = \begin{bmatrix} \beta(\eta_x u + \eta_y v + \eta_z w) \\ \eta_x(p + u^2) + \eta_y uv + \eta_z uw \\ \eta_x uv + \eta_y(p + v^2) + \eta_z vw \\ \eta_x uw + \eta_y vw + \eta_z(p + w^2) \end{bmatrix}, \quad f_{v1} = \begin{bmatrix} 0 \\ \eta_x \tau_{xx} + \eta_y \tau_{xy} + \eta_z \tau_{xz} \\ \eta_x \tau_{xy} + \eta_y \tau_{yy} + \eta_z \tau_{yz} \\ \eta_x \tau_{xz} + \eta_y \tau_{yz} + \eta_z \tau_{zz} \end{bmatrix},$$

$$g_1 = \begin{bmatrix} \beta(\zeta_x u + \zeta_y v + \zeta_z w) \\ \zeta_x(p + u^2) + \zeta_y uv + \zeta_z uw \\ \zeta_x uv + \zeta_y(p + v^2) + \zeta_z vw \\ \zeta_x uw + \zeta_y vw + \zeta_z(p + w^2) \end{bmatrix}, \quad g_{v1} = \begin{bmatrix} 0 \\ \zeta_x \tau_{xx} + \zeta_y \tau_{xy} + \zeta_z \tau_{xz} \\ \zeta_x \tau_{xy} + \zeta_y \tau_{yy} + \zeta_z \tau_{yz} \\ \zeta_x \tau_{xz} + \zeta_y \tau_{yz} + \zeta_z \tau_{zz} \end{bmatrix}$$

There are physical and numerical advantages to using the method of artificial compressibility [35]. Physically, the pressure becomes directly coupled to the governing equations through the artificial compressibility term (26). Most primitive variable solution schemes require the solution of Poisson's equation for pressure at the end of each iteration, resulting in an indirect coupling of pressure to the rest of the flowfield [34]. The direct relationship established by the artificial compressibility

term is not only more physically realistic, but it also speeds up convergence because Poisson's equation no longer needs to be solved each iteration. This dramatically reduces CPU time per iteration. In addition to speeding up convergence, the addition of artificial compressibility also changes the form of the equations from a mixed elliptic-parabolic set to one of a pure hyperbolic nature [35]. The hyperbolic classification opens up the possibility of upwind differencing and the use of marching schemes to solve the equations. These details are the subject of the following sections.

### 3.3 DIFFERENCING

Before the flow equations can be solved numerically, the partial derivatives must be approximated in some manner. One widely used representation of the partials in the aerospace field is the finite difference approximation. Such an approximation does two things: the flowfield is transformed from a continuum to a discrete set of points, and the partial derivatives are replaced by algebraic expressions based on Taylor Series expansions. These two results allow approximate flow solutions to be obtained that would otherwise be impossible. The differencing schemes used in the INS3D-UP code are discussed here.

#### 3.3.1 Transformation Metrics

As previously discussed, analytic expressions for the transformation metrics (10) are generally not known. Therefore some approximations must be made. As with the governing equations, it is convenient to compute the metrics using finite difference expressions. This allows the choice of any right-handed, body-fitted coordinate system in the physical domain as well as a uniform, orthogonal grid in the computational domain. For a grid that does not vary with time, a second-order

central difference can be used to compute the partial derivatives in the metrics. Equation (28) is such an example for a uniform, orthogonal grid.

$$x_{\xi} = \frac{\partial x_{i,j,k}}{\partial \xi} = \frac{1}{2\Delta\xi}(x_{i+1,j,k} - x_{i-1,j,k}) \quad (28)$$

The individual partials can then be spatially averaged to form the metrics. For example, if an average operator  $\mu$  is defined as

$$\mu_{\xi} x_{i,j,k} = \frac{1}{2\Delta\xi}(x_{i+1,j,k} - x_{i-1,j,k}) \quad (29)$$

then the final form of the metrics becomes [35]

$$\xi_x = \mu_{\xi}(y_{\eta})\mu_{\eta}(z_{\xi}) - \mu_{\eta}(y_{\xi})\mu_{\xi}(z_{\eta}) \quad (30)$$

### 3.3.2 Pseudo-Time Derivatives

The flow equations are solved by marching in pseudo-time until a steady-state solution is reached. Therefore a representation of the pseudo-time derivatives is required. The flow equations have been put in the following form (Section 3.2):

$$\frac{\partial U_1}{\partial \tau} + \frac{\partial E_1}{\partial \xi} + \frac{\partial F_1}{\partial \eta} + \frac{\partial G_1}{\partial \zeta} = 0 \quad (31)$$

or

$$\frac{\partial U_1}{\partial \tau} = -R \quad (32)$$

where

$$R = \frac{\partial E_1}{\partial \xi} + \frac{\partial F_1}{\partial \eta} + \frac{\partial G_1}{\partial \zeta} \quad (33)$$

The pseudo-time derivative can be replaced with a simple, implicit Euler difference since accuracy in pseudo-time is not required [35].

$$\frac{\Delta U_1^{n+1}}{\Delta \tau} = -R^{n+1}, \quad \Delta U_1^{n+1} = U_1^{n+1} - U_1^n \quad (34)$$

where  $n$  represents the pseudo-time level. The right hand side of (34) is then linearized to give

$$\left[ \frac{I}{J\Delta \tau} + \left( \frac{\partial R}{\partial U} \right)^n \right] (U^{n+1} - U^n) = -R^n \quad (35)$$

where  $I$  is a 4x4 identity matrix. The details regarding the formation of  $R^n$  and the solution of the equations are left to subsequent sections.

### 3.3.3 Convective Flux Differencing

In the previous section, the residual term,  $R^n$ , was defined as

$$R^n = \frac{\partial E_1^n}{\partial \xi} + \frac{\partial F_1^n}{\partial \eta} + \frac{\partial G_1^n}{\partial \zeta} \quad (36)$$

where

$$E_1 = \frac{e_1 - e_{v1}}{J}, \quad F_1 = \frac{f_1 - f_{v1}}{J}, \quad G_1 = \frac{g_1 - g_{v1}}{J} \quad (23)$$

and

$$\frac{\partial E_1}{\partial \xi} = \frac{1}{J} \left( \frac{\partial e_1}{\partial \xi} - \frac{\partial e_{v1}}{\partial \xi} \right), \text{etc.} \quad (37)$$

This section will only cover the convective terms while the viscous terms are discussed in the following section. The convective terms are represented using an upwind difference formulation. This scheme expedites convergence and also increases the robustness of the code [35]. CFD codes that utilize central differencing typically require the addition of numerical dissipation to damp out numerical oscillations caused by the non-linear convective fluxes. This has been a problem facing the CFD community for years since the amount of dissipation added can influence the final solution. Upwind differencing, however, provides implicit dissipation to the equations, removing the need for any explicit, user-supplied dissipation. Also, an upwind scheme contributes to the diagonal term of the Jacobian of the residual, making the scheme nearly diagonally dominant [35]. A diagonally dominant matrix is much easier to numerically solve than a non-diagonally dominant matrix. The upwind scheme used in INS3D-UP employs flux difference splitting based on the sign of the eigenvalues of the convective flux Jacobian [35]. The details that follow are based on Roe's method for solving the compressible gas dynamic equations [41] and are taken from Rogers [35].

Each dimension of the problem is considered separately as follows:

$$\frac{\partial e_1}{\partial \xi} = \frac{\hat{e}_{i+1/2} - \hat{e}_{i-1/2}}{\Delta \xi} \quad (38)$$

where  $\hat{e}$  is a numerical flux given by

$$\hat{e}_{i+1/2} = \frac{1}{2} [E_1(U_{i+1}) + E_1(U_i) - \phi_{i+1/2}] \quad (39)$$

$E_1(U_i)$  is the value of  $E_1$  obtained using the values of the primitive variables at  $U_i$ .  $\phi_{i+1/2}$  is a dissipation term. A first order upwind scheme results if  $\phi_{i+1/2}$  is defined such that

$$\phi_{i+1/2} = \Delta E_{i+1/2}^+ - \Delta E_{i+1/2}^- \quad (40)$$

where  $\Delta E^*$  is the flux difference across  $\pm$  traveling waves. The flux difference can be evaluated if the following definitions are established

$$\bar{U} = \frac{1}{2}(U_{i+1} + U_i), \quad U_{i+1/2} = U_{i+1} - U_i \quad (41)$$

and if the similarity transformation is considered. The Jacobian can be expressed as

$$A = X\Lambda X^{-1} \quad (42)$$

if  $\Lambda$  is the matrix with the eigenvalues of  $A$  on the main diagonal and zeros off the diagonal, and  $X$  is the matrix of eigenvectors of  $A$ . Since the eigenvalues of  $A$  correspond to the slopes of the characteristics, the direction of information propagation is determined by the signs of the eigenvalues. To model this phenomena in a physically meaningful fashion, it is necessary to distinguish between positively and negatively sloped characteristics (this is also necessary for numerical stability). Therefore, consider the following splitting of the eigenvalue matrix:

$$A^+ = X\Lambda^+X^{-1}, \quad A^- = X\Lambda^-X^{-1} \quad (43)$$

where  $\Lambda^\pm$  is the matrix containing the  $\pm$  eigenvalues. This splitting allows appropriate differencing based on the local direction of information propagation. Now the flux difference can be computed by

$$\Delta E_{i+1/2}^\pm = A^\pm(\bar{U})\Delta U_{i+1/2} \quad (44)$$

Examples of higher order schemes, as well as the complete eigenstructure of  $A$ , can be found in Rogers [35].

### 3.3.4 Viscous Flux Differencing

The final components of the residual are the viscous flux terms. These terms are differenced using second order central differencing in the INS3D-UP code. For example

$$\frac{\partial e_{v1}}{\partial \xi} = \frac{e_{v1+1/2,j,k} - e_{v1-1/2,j,k}}{\Delta \xi} \quad (45)$$

where the values at the half-points are obtained by averaging neighboring values.

$$e_{i+1/2} = \frac{1}{2}(e_{i+1} + e_i) \quad (46)$$

## 3.4 IMPLICIT SCHEME

The flow Equation (35) is numerically solved using a block Gauss-Seidel iterative scheme with line-relaxation. The solver sweeps through the computational domain with varying direction. All of the terms along the current line are solved for

implicitly, while the terms not on the sweep line are multiplied by the current  $\Delta U_1^n$  and moved to the right hand side. The direction of the sweeps alternates as prescribed by the user until the residual and the divergence of the flowfield approach zero. This solution strategy follows that outlined by MacCormack [42].

All of the information in Equation (35) is known except for the  $\Delta U_1^{n+1}$  term. The Jacobian of the residual vector is computationally very expensive to form, so it is approximated as described by Rogers [35]. At each iteration the  $\Delta U_1^{n+1}$  term is solved implicitly. When  $\Delta U_1^{n+1}$  is known, the flow variables can be updated using Equation (34).

## CHAPTER 4

### COMPUTATIONAL GRIDS AND BOUNDARY CONDITIONS

#### 4.1 INTRODUCTION

This chapter covers the information relevant to the building of the computational meshes. Before the grids are discussed, a description of the geometries that were studied is included. An overview of the general grid building scheme, as well as a description of the grid building tools, makes up the third section of this chapter. Section 4.3 contains the information common to all of the grids that were built. Specific details for each grid are discussed in the sections dedicated to airfoil, full-span, and half-span grids. The final section identifies the different boundary conditions used in this simulation.

#### 4.2 GEOMETRY

The geometries studied were all based on the NACA 632-215 Mod. B airfoil section [43]. This airfoil was fitted with two different riggings of a 30% Fowler flap. Figures 5-7 show the airfoil section with and without the flap elements. The two flap riggings studied were representative of a take-off and landing configuration. The rigging details are contained in Table 1. Both configurations were set at 10 degrees angle of attack.

Condition	Deflection (deg.)	Gap/Chord	Overlap/Chord
Take-off	10.0	0.030	0.042
Landing	30.0	0.023	-0.0039

Table 1, Flap Rigging Parameters.

The gap and overlap are defined in Figure 8 and are expressed in units of unflapped airfoil chord. As shown, the gap is defined as the vertical distance between the

lower surface of the trailing edge and the highest point on the deflected flap element. Overlap is the horizontal distance between the main element trailing edge and the leading edge of the deflected flap. It is defined so that in a configuration with negative overlap the flap is positioned completely downstream of the main element.

The full-span flap cases are a simple extrusion of the airfoil into a wing for which all of the spanwise stations are identical. The wing fully spans a modeled wind tunnel test section. The test section is modeled after the NASA Ames 7-by-10 Foot Wind Tunnel with the false wall discussed by Storms and Ross [14]. The half-span flap cases consist of the flapped airfoil over half of the tunnel span with the unflapped section composing the second half of the span. The half-span flap geometry is shown in Figure 9.

#### 4.3 GRID BUILDING PROCESS

The grid building process begins by creating a surface grid from a surface definition. The difference between the surface definition and grid is largely a matter of detail. A surface definition consists of enough information ( $x, y, z$  locations) to completely and accurately define the surface shape, whereas a surface grid contains specific refinement needed to resolve the desired flow features. Also, in the case of a C-grid, as used for the wing section grids, a wake cut is part of the surface grid. All of the surface grids in this study were created in two-dimensions and extruded into three-dimensions where necessary.

The next step is to create a volume grid. The hyperbolic grid generator HYPGEN [44] was used for the grids in this study. HYPGEN begins at the surface and creates the volume grid by marching outward a prescribed distance using the solution of hyperbolic partial differential equations. The solution to these partial differential equations must satisfy two orthogonality relationships and one cell

volume constraint [44]. A volume grid is generated in this fashion for each airfoil element. An example of this can be seen in Figure 10.

The final overset grid was created using the PEGSUS code [45]. PEGSUS is based on the Chimera scheme of Benek, Buning, and Steger [46]. The Chimera scheme provides one method of joining individually generated grid zones into a single region. As part of the merging process, communication must be established between the zones so that each grid can be influenced by neighboring regions. Also, grid points in overlapping regions that do not make physical sense need to be removed from the computational domain. For example, grid points in one zone should not fall inside a solid surface of another zone. This is illustrated in Figure 11.

In the Chimera approach, the grid zones communicate with one another through an explicit interpolation scheme. This interpolation occurs at grid boundaries, imposing a type of boundary condition. Each boundary point is updated by interpolating flow information from a surrounding cell in an overlapping zone. In Figure 12, point *A* is updated by interpolation flow information from the points marked *B*. At least one cell of overlap is needed for this interpolation link to be established by PEGSUS. The flow variables at the points requiring interpolation are updated after each flow solver iteration. This approach ensures a smooth solution across the boundaries, but does slow convergence due to changing values at the boundaries.

PEGSUS allows the user to “cut holes” in a mesh to prevent non-physical situations as illustrated in Figure 11. When a hole is “cut” all of the points falling within the hole boundaries are removed from the computational domain. Each grid point contains an integer flag, in addition to the coordinates of the point, known as the *Iblank* value. For a normal point inside the computational domain, *Iblank* is set to one. When a point is removed as part of a hole, its *Iblank* value is set to zero (the point is said to have been blanked). A zero *Iblank* value flags the flow solver to

ignore this point when looping through the grid. An example of how holes are used to avoid problems in overlap regions is shown in Figure 13. The points that were previously inside the solid boundary have now been blanked and no longer appear in the computational domain. Since the grid in which the hole was cut is no longer continuous, Figure 14, additional information must be provided at the boundary of the hole. These points are known as fringe points. The flow variables at the fringe points are found by interpolating from other grids in the manner described above. Care must be taken when defining the holes so that at least one cell of overlap exists at all hole boundaries. In Figure 12 sufficient overlap exists, and point *A* will be updated by interpolating the values at the four *B* points.

The grids are merged and interpolation stencils are formed by the PEGSUS code. The user provides the individual grids and a PEGSUS input file. The input file contains the definition of hole and outer boundaries in addition to zone location information. Using the zone positioning capabilities of PEGSUS, individual zones can be translated and rotated so that they are correctly placed with respect to the other zones. In this study, the model angle of attack was set using this feature. An interpolation database is created for all of the points that require updating by interpolation and is written to a file. The multi-grid and interpolation database files are used by the flow solver.

#### 4.4 AIRFOIL GRIDS

The grids used in this study were modeled after those used by Carrannanto et al. in his study of multi-element airfoils [23]. In this study, however, wind tunnel walls were also modeled in the computations. This was done to obtain results that would be more directly comparable with wind test results. C-grids were used to model the airfoil elements and an H-grid was used to model the wind tunnel walls. A grid resolution study was performed to investigate the effects of grid density on

the flow solution and to establish grid density requirements for the three-dimensional work. It was found that the resolution used by Carrannanto et al. was adequate to resolve the flow physics up to angles of attack near  $C_{lmax}$ . Since it was desired to have the same cross-sectional grid for the two- and three-dimensional cases, and since the grid size must be kept as small as practical for three-dimensional studies, no grid points were added.

The grid sizes for the main and flap elements were  $227 \times 80$  and  $155 \times 59$  respectively. The circumferential grid spacing was  $10^{-3}$  chords at the trailing edge of both elements. The wall spacing was  $10^{-5}$  chords ( $y^+_{ave} \approx 1$ ) for both of these zones. In the normal direction, the main element grid extended approximately two chords while the flap grid was on the order of 0.15 chords. Wake cuts extended 2.5 chords downstream for the main element and 0.3 chords for the flap. The wake cuts for both elements were located in the manner suggested by Carrannanto et al. The wake of the main element followed the upper surface of the flap and was offset by the gap between the elements (see Figure 15). Once aft of the flap element, the wake cut made a straight line parallel to the chord of the deflected flap. The wake cut of the flap grid extended from the trailing edge of the flap along the flap chord line. Elliptic smoothing was applied to the flap grid aft of the flap trailing edge as suggested by Carrannanto et al. Smoothing expands the circumferential grid lines in the vicinity of the wake cut, reducing the aspect ratio of the grid cells in this region. The result is accelerated convergence and improved interpolation between grid zones [23]. Trailing edge thickness was neglected in the computations for both elements. It was felt that any effects of the blunt trailing edges would be local in nature and would not reduce the overall accuracy of the computations. More recent results have confirmed this assumption [47].

The wind tunnel grid was designed for computing the effects of inviscid wind tunnel walls on the model. The size of the grid was  $85 \times 30$ , and resolution studies

showed very little sensitivity to the dimensions of this grid. The grid extended  $\pm 15$  chords in the streamwise direction. The walls were located two chords above and below the center of the airfoil at zero degrees angle of attack. The vertical distance between the walls was constant along the length of the tunnel grid. The physical wind tunnel walls diverge slightly through the test section to account for the growth of the boundary layer, and this divergence was neglected in the computations.

The three zones were combined into a two-dimensional multi-zone using PEGSUS. The complete grid contained approximately 30,000 grid points. An example of an airfoil grid can be seen in Figure 16. This grid represents the landing configuration at ten degrees angle of attack.

#### 4.5 FULL SPAN FLAP GRIDS

The full-span flap grids provided a direct extension of the airfoil work into three-dimensions. The two-dimensional planes were copied and stacked together in a spanwise row to form a three-dimensional grid prior to the merging of the zones using PEGSUS. This allowed for different spanwise resolution in each zone. The work in two-dimensions allowed all of the Chimera details to be worked out prior to creating the three-dimensional grid. This offered significant savings of both time and computer resources. Part of the reason for studying this configuration was to determine the number of spanwise planes needed to resolve any three dimensional flow. As the study progressed, no strong effect of spanwise resolution was seen for this case. The final grid sizes were  $227 \times 30 \times 80$ ,  $155 \times 30 \times 59$ , and  $85 \times 30 \times 30$ , for a total of 900,000 points. The physical spanwise dimension was determined by the wind tunnel size, including the presence of false walls needed for the experiment [14]. The span of the grid was 2 chords.

#### 4.6 HALF SPAN FLAP GRIDS

The half-span grid was composed of six zones. Cross sections of three of these zones, the flapped main element, flap element, and wind tunnel grid, were identical to those used in the two-dimensional computations. The flapped part of the wing extended from the mid-span of the tunnel to a wind tunnel wall. The other half of the tunnel was spanned by the unflapped wing element. This cross section was modeled using a C-grid of dimensions 185X52. As with the other wing sections, the wall spacing was  $10^{-5}$  chords with a circumferential trailing edge spacing of  $10^{-3}$  chords. The wake cut of this grid extended 2.5 chords behind the wing in a direction parallel to the section chord. The outer boundaries were located a normal distance of two chords from the surface.

The remaining two zones were needed to model additional solid boundaries. One such surface was the exposed region where the flapped main element met the unflapped main element at the mid-span. The flapped section has a smaller chord than the unflapped section as well as a cut-out, or cove, region where the flap is stowed when the high-lift system is not in use. When the flap is deployed, this mismatch area is exposed and must be modeled. Figure 17 illustrates the location of this surface. The grid used to represent this surface was an H-grid deformed to match the airfoil contours. This grid is hereafter referred to as the patch grid. As with all of the grids, the patch grid was initially generated as a two-dimensional plane. The plane contained 33x33 grid points. Figure 18 shows a patch grid plane. The final zone was needed to model the flap edge surface. The grid used to do this was also an H-grid deformed to match the flap cross section. This plane contained 36x40 points. A flap edge grid plane is shown in Figure 19. Both of these grids were expanded outward to establish an overlap region so that interpolation could occur.

As with the full-span flap case, all of the grid planes were copied into spanwise stacks to fill out the third dimension. Forty spanwise grid planes were

used for the following grid zones: flapped and unflapped main elements, flap element, and wind tunnel. The patch and flap edge grid zones each contained ten spanwise planes. The three dimensional grids were then passed to PEGSUS for merging and establishing the interpolation links between the zones. Proper Chimera interpolation between grids proved a challenge in two locations; the overlap region between the flapped and unflapped main elements and the flap edge region.

The mid-span location was complicated because two grids of different shapes were required to fit together and communicate. As mentioned, the shape difference between the main element sections was corrected through the use of the patch grid. The first spanwise plane of the patch grid was located at the solid surface, coincident with an unflapped grid plane, and the grid was marched  $1.5 \times 10^{-3}$  chords into the flapped portion of the grid. The interpolation between the main element grids was more difficult to establish. The unflapped main element extended  $10^{-3}$  chords and four grid planes into the flapped element grid. This overlap allowed the end planes of each grid to receive interpolated information from the interior of the other grid. This overlap created an additional problem, however. The inner plane of a C-grid is a computational boundary, hence requires boundary information for a solution to exist. For the most part, the flapped and unflapped surfaces were coincident, so solid surface boundary conditions could be used. Near the trailing edge, this approach did not work because a portion of the flowfield in one grid (flapped main element) would have coincided with a solid surface in the other grid (unflapped main element). This would have created an inconsistency in the solution. To circumvent this, the portion of the unflapped trailing edge that extended into the computational domain of the flapped grid was defined as a Chimera boundary, and thus was updated by interpolation. Figure 20 shows a cross section of the grid in the overlap region with the appropriate boundary conditions shown.

The flap edge region was simpler to set up, but turned out to play an important role in the convergence of the solution. The first approach was to place the last grid plane of the flap edge grid at the solid surface and march the grid away from the surface as was done with the patch grid. Using this grid scheme, the solution would not converge. This was traced to an unsteady flow separation occurring at the corner of the flap edge and flap surface. The flap edge grid was not able to resolve this feature with only boundary information. The problem was fixed by extending the flap edge grid three grid planes into the flap surface. The points inside the surface were blanked from the computation and the solid surface boundary condition was applied to the plane that was third from the end of the grid. This allowed the flap edge grid to resolve the flow separation at the corner, and the solution converged.

No grid resolution study was performed for this grid due to the computational requirements for a single solution. Because the solution captured small scale flow features, such as secondary separations at the flap edge, the resolution appeared sufficient for this study. The final grid contained 1.8 million grid points. Figure 21 shows the final surface grid for the half-span flap geometry in a landing configuration.

#### 4.7 BOUNDARY CONDITIONS

All of the solid surface points on the wing were modeled using a no-slip boundary condition. This condition specifies zero velocity and a zero normal pressure gradient at the surface. Because a C-grid topology was used, wake-cut boundary conditions were also needed. Wake points are updated by a first order averaging of the points on either side of the wake cut. The wind tunnel walls were represented by slip-walls which impose a zero normal gradient for all flow variables. The tunnel inflow condition was prescribed with uniform normal velocity

and constant total pressure. The outflow of the tunnel consists of a constant static pressure and extrapolated velocity. The outer boundaries of all grid zones falling inside the wind tunnel grid were Chimera boundaries.

## CHAPTER 5

### RESULTS AND DISCUSSION

#### 5.1 INTRODUCTION

This chapter includes a presentation of the results of this research. The Airfoil Results section establishes a starting point for this study. Much initial work was done in two-dimensions due to the faster turn around time associated with this simplified problem. The full-span flap investigations provided a good validation case for the three-dimensional flow solver. This case also allowed for the evaluation of the grid development work performed in two-dimensions. The final section of this chapter provides a discussion of the interesting results seen in the half-span flap computations. Specific attention is given to the differences between the full- and half-span cases.

#### 5.2 TWO-DIMENSIONAL AIRFOIL RESULTS

To make comparisons between solutions meaningful, it was important to establish a convergence criteria so that all solutions could be converged to the same level. The INS2D-UP codes writes the maximum divergence of velocity value at each iteration. From a physical point of view, the divergence represents how well mass is conserved for the incompressible flowfield. With the artificial compressibility term added to the continuity equation, the divergence values indicate the levels of unsteadiness in the solution. As the divergence approaches zero, the solution approaches steady-state. For this work, the solution was iterated until the divergence of velocity fell to the order of 0.1. This typically corresponded to a residual reduction of five orders of magnitude. Convergence was reached in 300-500 iterations for angles of attack below  $C_{lmax}$ . Near stall, up to 1200 iterations were sometimes required to obtain a steady-state solution due to the inherent

unsteadiness in the flow. No computations were performed beyond stall. A 500 iteration run using 30,000 grid points required approximately eight minutes of CPU time on a Cray C-90 supercomputer.

The computed two-dimensional results are compared to data taken in an unpublished study at NASA Ames Research Center. The experiment occurred in the U. S. Army 7- by 10- Foot Wind Tunnel. The flow conditions for the test were freestream  $M_\infty = 0.2$  and  $Re = 3.7 \times 10^6$  based on the undeflected airfoil chord. The model had an unflapped chord of 2.5 feet. Due to mounting hardware, false walls were placed in the tunnel, reducing the effective test section span from seven to five feet. The lift coefficients were computed from an integration of pressures measured at the model mid-span. Boundary layer control was used at both walls to maintain two-dimensional flow at the wing-wall junction. Three blowing slots were located on each side wall, two above the upper surface of the main element and one above the upper surface of the flap. Air was injected along the wall parallel to the wing surface. The blowing rate was adjusted until the pressures at three spanwise stations agreed. The data used for comparison was not corrected for any wind tunnel wall effects.

Figure 22 shows the variation of lift coefficient with angle of attack for the  $10^\circ$  flap deflection (take-off) case. The agreement between computations and the experimental data is quite good up to stall. Stall is not accurately computed due to a lack of circumferential grid resolution on the main element [47]. Stall on a flapped airfoil typically occurs when the separation point on the main element suddenly shifts forward with a small increase in angle of attack. The relatively sparse grid resolution along the mid-chord region of the airfoil prevents the accurate computation of this separation point shift. Higher grid resolution has shown to cure this problem [47], but would not be practical in the three-dimensional computations.

The computed results show a slight decrease in lift-curve slope compared to the experiment. Also, an offset of 0.1 in  $C_l$  is seen at zero angle of attack.

A similar plot for the  $30^\circ$  flap deflection (landing) case is shown in Figure 23. The trends are similar to those shown for the take-off configuration. The most notable difference between Figure 22 and Figure 23 is the increased offset between experiment and computations in the landing case. The offset between the curves is 0.3 in  $C_l$  at zero degrees angle of attack.

Figures 24-27 present comparisons of computed and experimental pressure distributions. Figure 24 shows the pressure distributions for the take-off configuration at  $0^\circ$  angle of attack. The agreement is good over the upper surface of the main element, but on the lower surface the agreement is poor. This was an unexpected result because the flow on the lower surface is largely potential and is usually relatively easy to predict accurately. For example, the two-dimensional version of the potential flow code PMARC was used to compute the pressures about this geometry without wind tunnel walls [48]. Figure 28 shows the resulting comparison. The PMARC results agree very well with the INS2D-UP results. The fact that these two very different methods gave such similar results provides confidence in the computational results. Also, INS2D-UP has proven the ability to accurately model multi-element airfoils in many cases [20-23]. This would suggest two possible sources of the disagreement: an error in the experimental data exists or there was some difference between the experimental and computational conditions. The overall agreement on the flap element is much better than on the main element. The most noticeable difference occurs on the upper surface at the trailing edge. The experiment shows a sudden pressure coefficient ( $C_p$ ) increase at the most aft pressure tap. The computed results do not show this because no trailing edge bluntness was modeled. Ashby has verified that trailing edge bluntness is the source of this disagreement [47]. The suction peaks are captured for both elements.

The agreement appears much better for the  $\alpha=10^\circ$  case shown in Figure 25. The only visible disagreement is in the area of the suction peak on the main element. INS2D-UP slightly under predicted the value of maximum suction. This small difference could be attributed to local compressibility in the experiment which is not present in the computations.

The landing configuration cases, Figures 26-27, show results similar to those discussed above. However, the discrepancy between the CFD and experiment is visible on both the upper and lower surfaces for  $\alpha=0^\circ$ . As with the take-off flap deflection, the agreement improves at the higher angle of attack. A suction spike is visible at the leading edge of the main element in Figure 27. This is a local phenomena caused by a discontinuity in the curvature of the surface grid. Figure 29 shows a plot of the second derivatives of the airfoil surface. The closer the curvature discontinuity is to the suction peak, the more noticeable the pressure spike becomes. A similar phenomena occurs on the flap element but is less noticeable because of its lower magnitude.

### 5.3 FULL-SPAN FLAP RESULTS

The full-span flap case provided a logical transition point from the two-dimensional airfoil work to a three-dimensional study. The goal of this phase of the research was to gain confidence in the ability of INS3D-UP to predict high-lift flows while simultaneously studying the effects of spanwise grid density. It was also hoped that any inherent differences between INS2D-UP and INS3D-UP would be apparent. These comparisons could be used to gain insight into the effects of wind tunnel walls and three-dimensional turbulence in two-dimensional wind tunnel testing. A full-span flap solution required 600 iterations to converge. For this case, convergence was set at the point where the divergence of velocity fell below unity. A slightly less stringent convergence criteria was used in three dimensions due to

the increase in computational requirements. Convergence took 12 hours on a Cray C-90 supercomputer.

The two-dimensionality of the full-span result can be seen in Figure 30. This figure shows the pressure distribution for three spanwise stations. The computed pressures are the same at every spanwise location. The pressures did not change with varying spanwise grid density. Even in regions of separated flow, the pressures did not change noticeably, and the spanwise velocity perturbations were so small in magnitude that the flow remained essentially two-dimensional. This can be attributed to several factors. Most importantly, the grid planes were identical at every spanwise station. No physical wing is geometrically identical along its span, and these slight surface variations introduce three-dimensional disturbances into the flow. Turbulence itself is also inherently three-dimensional in nature. In a real, separated flow, the presence of turbulence is enough to generate a three-dimensional velocity field. Because CFD requires the use of turbulence models, some of the three-dimensionality of turbulence is lost. This is because the models are designed to approximate the eddy viscosity of turbulence, not the physical fluctuations in the flow. The fact that inviscid walls were modeled in the computations removed another possible source of three-dimensional flow disturbances. A wall with a boundary layer that impinges on the model has the possibility of introducing spanwise velocity perturbations. With an inviscid wall, no boundary layer was present, so two-dimensional flow was maintained at the wall.

The pressure distributions computed with INS3D-UP are compared with the INS2D-UP results in Figure 31. As shown, the two codes predict nearly identical pressure distributions for this geometry. Figure 32, shows a good comparison between experimental and computed pressures. Since the full-span flap results so closely match the two-dimensional results, it is expected that other configurations would show the trends discussed in Section 5.2. This demonstrated that there were

no fundamental disagreements between the INS2D-UP and INS3D-UP codes, giving some confidence that INS3D-UP could predict high-lift flows. Also, the results suggested that much work, such as grid studies, could be done in two-dimensions, greatly reducing the computational requirements. Because of these results, it was felt that no additional knowledge would be gained by computing additional full-span configurations.

#### 5.4 HALF-SPAN FLAP RESULTS

Solutions for the take-off and landing configurations at ten degrees angle of attack and a Reynolds number of 3.7 million were computed. In most instances, the effect of the flap edge was the same in both flowfields, but was exaggerated in the landing flap deflection case. Therefore the results presented are for the landing configuration unless specifically stated otherwise. Results from the take-off case are included where they differ significantly from those of the landing case. Both of these solutions were iterated until the flow divergence fell below one. A run required approximately 550 iterations and twenty-four Cray C-90 hours to converge.

Figure 33 provides a general view of the flowfield about the half-span flap wing in the landing configuration. This figure contains particle traces colored by velocity magnitude. The surface particles are restricted to the surface which would represent oil flow patterns in an experiment. The particle traces away from the surface are unconstrained. The blue regions represent velocities well above free stream, and the red areas are velocities close to free stream. This figure illustrates the large scale effects of the flap edge: the flap tip vortex, large amounts of spanwise flow, and separation lines can all be seen. Figure 34 shows the same particle traces for the take-off configuration. A weaker tip vortex is present and the amount of spanwise flow has decreased. The separation lines have also nearly disappeared.

The presence of the flap edge greatly modifies the lift distribution of the wing. Figures 35 and 36 show plots of the spanwise lift distribution for the landing and take-off configurations. In both cases, an abrupt change in lift is seen at the location of the flap edge. This change is caused by a discontinuity in the chord and camber distributions as the wing section changes from the unflapped to the flapped airfoil. For the landing case, the total section lift coefficient, referenced to the unflapped airfoil chord, changes by 0.3 at the flap edge. This change in circulation (lift) causes vorticity to be shed into the wake in the form of a tip vortex. This vortex in turn induces a velocity field which further modifies the lift. The induced velocity appears as upwash on the unflapped wing segment and as downwash on the flapped half of the wing. Upwash increases the local angle of attack which increases the lift. This explains why the lift coefficient on the unflapped side of the wing is much higher than the two-dimensional value at the same angle of attack. Conversely, the lift on the flapped half of the wing is much lower than its corresponding two-dimensional value. The effect of the vortex varies with the distance from the flap edge. If the wing span were extended infinitely in both directions, the lift coefficients would eventually return to the two-dimensional values.

The shape of the takeoff and landing lift distributions differ slightly in the vicinity of the flap edge. In the takeoff case (Figure 35), the lift on the flap varies across the span, while almost no change in lift occurs over the span in the landing case (Figure 36). The velocity induced by the tip vortex changes the local angle of attack across the span, and the sections nearest the tip are affected the most. The change in the angle of attack is responsible for the lift changes for the takeoff configuration. In the landing case, the presence of separated flow modifies the shape of the lift distribution. As the local angle of attack decreases near the flap edge, the separation point moves aft (Figure 33). The reduction in the amount of

separated flow causes an increase in the lift generated by the section. In this case, the lift gained by reducing the size of the separated region is very nearly the same magnitude as the decrease in lift due to the reduced angle of attack. Therefore, the lift on the flap remains nearly constant over the span.

The spanwise variation in lift is caused by variations in the pressure distributions. Figure 37 illustrates this phenomena for two stations along the unflapped half-span. The increased upwash nearest the flap edge (i.e. mid-span) has increased the effective angle of attack compared to the section near the wall, decreasing the pressure coefficients on the upper surface of the wing. A slight increase in the lower surface pressure coefficients at mid-span can also be seen. The most significant difference between the two pressure distributions shown in Figure 37 occurs at the trailing edge. The section closest to the flap edge displays a slightly negative pressure gradient at the trailing edge, while the section near the wall shows continuing pressure recovery all the way to the trailing edge. This can be explained by the high induced velocities at the trailing edge of the mid-span section. These induced velocities create a region of increased dumping velocity (the velocity at which the flow leaving the trailing edge must adjust to), decreasing the  $C_p$  to which the pressure must recover. For an airfoil without a flap, the trailing edge condition is such that the flow tends toward freestream as it leaves the airfoil surface. In a multi-element airfoil, the flow leaving the trailing edge of an upstream element often has the tendency to approach a velocity much higher than freestream due to the high velocities induced by the downstream element. The unflapped portion of the wing is more susceptible to this phenomena because of the exposed edge created by the mismatch in chord at the junction of the flapped and unflapped sections. In all cases, the pressure distributions for sections between the mid-span and the wall fall between the two curves shown in Figure 37.

Figure 38 shows a similar plot for the flapped main element section. In this case the upper surface  $C_p$ 's become more negative and the lower surface  $C_p$ 's become more positive as they move away from the mid-span toward the wall. As with the unflapped section, the largest differences are seen at the trailing edge. No upturn in the pressure distribution is seen at the trailing edge of the mid-span section in this case. The upper surface velocities at the flapped trailing edge must match the velocities on the upper surface of the unflapped portion of the wing. The upper surface pressures must adjust so that they are continuous across the junction between the flapped and unflapped sections. Also, the lower surface of the flapped trailing edge is perpendicular to the solid surface formed by the patch grid because the flapped chord is five percent shorter than the unflapped chord. This solid surface allows a pressure difference between the upper and lower surfaces upstream of the trailing edge. Away from the mid-span, the pressure distribution quickly begins to match the distribution at the wall.

The greatest variation of pressure distributions occurs on the flap element. Figure 39 shows pressure distributions for three spanwise locations; at the flap edge, 0.1 chord from the edge, and at the wall. At the flap edge, the pressures are dominated by the tip vortex which completely alters the shape of the distribution. As shown in the plot, the leading edge suction peak is suppressed at the flap edge. Away from the edge, the flow accelerates around the airfoil leading edge as it moves away from the stagnation point. On the edge, however, the flow is not forced to follow a path over the airfoil surface: it can move spanwise as well. In this case, the flow does move in a spanwise direction toward the edge as it leaves the stagnation point, relieving the suction peak. The magnitude of the relief varies with spanwise position. As seen in Figure 39, the peak has nearly reached the wall value at a distance of 0.1 chord from the edge. The velocities over the aft part of the airfoil's

upper surface are higher at the edge than near the wall. The tip vortex travels just above the upper surface, inducing a region of high speed flow.

A consequence of the spanwise pressure variations is a shifting of the separation point location along the span. In Figure 40 surface particle traces illustrate a separation line on the flap. The separation point is farthest forward at the wall and farthest aft at the tip. The separation location is closely related to the pressure distributions discussed in the previous paragraph. As was shown in Figure 39, the flap pressure recovery is steepest at the wall and almost non-existent at the flap edge. Also shown in Figure 40 is the location of the two-dimensional separation line for the flapped airfoil at the same angle of attack. At the wall, the two- and three-dimensional flows separate very close to the same chordwise position. The separation points are essentially the same due to the resemblance of the corresponding flap pressure distributions. Figure 41 shows the half-span flap pressure distribution at the wall compared to the two-dimensional pressures. Since the distributions are almost identical, it is not surprising that the separation points are in the same location. The total lift generated by these sections is different (Figure 35), which implies that the lift coefficients on the main elements must also be different. The different pressure distributions (different lift coefficients) would cause the wakes leaving the main element to be different in both cases. Since the flap pressures and separation points are nearly the same, it can be concluded that the flap boundary layer in this case is not sensitive to small changes in the main element wake.

Figure 42 shows a comparison of the two and three-dimensional separation lines for the unflapped half-span. For this portion of the wing, the two-dimensional separation point is farther aft than the three-dimensional separation point at the wall. This is an expected result because the three-dimensional section is operating at a higher lift-coefficient than the two-dimensional section due to the upwash induced

by the tip vortex. For a given geometry higher lift usually results in earlier separation. Figure 43 shows a comparison of the wing surface pressures at the wall with the airfoil pressures. The steeper upper surface pressure recovery of the three-dimensional case is clearly the cause of the earlier boundary layer separation. Near the mid-span, however, the three-dimensional separation point is aft of the two-dimensional point, even though the three-dimensional section is generating more lift. The favorable pressure gradient at the trailing edge of the mid-span section, seen in Figure 37, enables the boundary layer to remain attached longer than in the two-dimensional case. Very close to the mid-span no clear separation line can be seen, as there is a large region of spanwise flow.

Figures 44-46 show the spanwise variation of pressure distributions for the take-off configuration. Figures 44 and 45, which show the pressures for the main element segments, are very similar to Figures 37 and 38. The differences across the span are less apparent for the take-off configuration. This is expected because the trailing vortex is weaker for the take-off case than it is for the landing case: the vortex strength is proportional to the lift on the flap which is higher for the landing configuration. The flap pressures do differ between the take-off and landing configurations. Figure 46 shows the variation of pressure coefficients over the span of the flap. Not only is the shape of the distribution at the edge different, but the effect of the edge is felt farther away from the edge in the landing case. The pressures 0.1 chord from the edge in the take-off case resemble the wall pressures more closely than those at the wall in the landing case. This is expected because of the weaker tip vortex in the take-off case. The leading edge pressures are suppressed more in the take-off configuration. The pressure coefficients decrease over the aft two thirds of the flap due to the presence of the tip vortex above the surface. As in the landing case, the vortex induces a high local velocity near the flap

edge, reducing the pressure. From Figure 46 it appears that most of the lift on the flap near the edge is vortex induced.

The tip vortex primarily responsible for the differences between the two and three-dimensional flows is created by the sudden change in circulation that occurs at the flap edge. Physically, the vortex arises from the pressure imbalance between the upper and lower surfaces of the flap. High pressure flow on the lower surface of the flap moves around the flap edge toward the low pressure region on the upper surface. This rotational flow structure is convected downstream by the local flow velocity which turns the structure into a vortex filament. Since the pressure difference between the upper and lower surfaces imparted angular momentum to the vortex, it has a tendency to continue to rotate until it is damped out by the fluid viscosity. This vortex decay usually occurs far downstream of the wing tip which created the vortex.

Figure 47 illustrates the location of eight positions over the upper surface of the flap investigated using particle traces. Figures 48-55 show the particle traces for these eight stations. The particles are restricted to the planes shown, so the plots contain projections of the streamlines onto the planes. In Figure 48 the vortex is not yet apparent, but the flow can be seen to travel parallel to the flap edge and around the corner onto the flap surface. The first signs of a vortex core are visible in Figure 49. The vortex filament is seen to increase in size as it progresses downstream (Figures 50-55), and it remains above the flap from its beginning to the trailing edge. The flow patterns shown in Figures 48-55 correspond to the surface flow patterns shown in Figure 40. The flow on the surface moves away from the flap edge before the vortex core is present. After the vortex appears above the surface, it induces a velocity beneath it towards the flap edge. The particle traces in Figure 40 show the changing direction of the flow near the flap edge due to the vortex. The vortex for the take-off flap deflection travels along a similar path.

It appears that leading edge flow near the flap edge moves in the spanwise direction toward the flap edge. The flow separates at the flap edge forming a small recirculation region. The blue particle traces near the leading edge in Figure 56 show the recirculation region. Fluid particles not caught in the recirculation region turn so that they flow along the flap edge. The particles begin to move towards the upper surface as they feel the influence of the flow leaving the lower surface. This can be seen in Figure 56. When they reach the upper surface, the particles form another small separation bubble as they flow around the corner formed by the upper surface and the flap edge. It is believed that this high vorticity bubble is the beginning of the vortex core. The bubble is barely visible at the corner in Figure 47.

An aspect of the flow that demonstrates the resolution provided by the flap edge grid is the secondary recirculation regions seen in Figure 57. These flow structures are fed by the fluid leaving the upper and lower surfaces at the flap edge. The flap edge grid did a good job of resolving the flow in this region, but its small size made the interpretation of the results difficult. Much of the interesting flow physics occurs across the boundaries of the flap edge grid, requiring the tracking of the flow from one grid zone to another. Since the grid resolutions are somewhat different in each zone, smooth transitions between zones is not always possible. The other drawback with the current flap edge grid is that a large number of Chimera boundaries occur in the region of highest flow activity. The information is passed between zones via a low-order interpolation scheme, so accuracy is lost in regions where the highest accuracy is desired. This also slows convergence somewhat which increases the required computer time for a given case. Ideally, the flap surface and edge would be modeled with a single zone.

Insufficient resolution has been identified in two regions of the grid. The vortex formation and dissipation were not adequately modeled by the current grid. The formation of the vortex is not well resolved due to a lack of spanwise and

chordwise grid density in the flap grid at this point. The spanwise spacing was kept at the current size so that adequate overlap could be obtained while keeping the overall grid size at a minimum. The chordwise spacing was determined from two-dimensional results, and the mid-chord region does not typically require many points to resolve for unseparated flows. In the current computations the trailing vortex is dissipated too quickly behind the wing. Accelerated decay occurs as the vortex travels into a portion of the grid that is not well resolved. The increasing cell size adds numerical dissipation to the solution which causes the vortex to damp out in a physically unrealistic fashion. Repositioning of the main element wake cut so that it follows the vortex path would better resolve the flow and may maintain the vortex in a more realistic manner. These grid modifications were not performed as part of this study.

## CHAPTER 6

### CONCLUSIONS AND RECOMMENDATIONS

A numerical investigation of a simple high-lift system was performed using an incompressible Navier-Stokes flow solver. The study began by investigating take-off and landing configurations of a two-element, two-dimensional airfoil at a range of angles of attack. Grid issues were addressed in two dimensions due to the much lower computational requirements. The two-dimensional grid planes were converted to a three-dimensional, full-span flap grid. This served as a validation case for the three-dimensional flow solver. Once confidence in the three-dimensional flow solver was established, a grid scheme was developed to model the effects of a half-span flap. The half-span flap case provided a means to study the flow physics associated with the flap edge.

The full-span results agreed well with experimental data for most cases. Some differences in the pressure distributions were seen between the computed and experimental results, particularly on the lower surface of the airfoil with high flap deflections. Because three computational techniques (INS2D-UP, INS3D-UP, and PMARC) produced very similar results, it is believed that the disagreement lies in an experimental error or in a modeling inconsistency between the experiment and the computations.

The grid scheme developed to represent the half-span flap configuration was successful. The grid provided enough resolution to capture the large-scale influence of the trailing vortex on the lift distribution of the wing. The change in the pressure distributions created large amounts of spanwise flow and modified the separation lines compared to the two-dimensional case. Secondary recirculation regions were seen in the solution at the corners formed between the flap surface and the flap edge.

The details of the tip vortex formation were not clearly seen in the current results, but the vortex trajectory could be followed over the upper surface of the flap once it has formed.

Findings from this research provided a number of possible extensions of this study. The effects of grid density at the flap edge could be investigated. An increase in the number of spanwise and chordwise points at the edge may show the formation of the tip vortex in more detail. Also, creating a single zone grid around the flap edge would better resolve the flow in this area without any uncertainty due to the Chimera boundaries. The wake cut of the main element could also be positioned so that it follows the trajectory of the tip vortex. This would make use of the large number of points along the wake cut and would more realistically model the convection of the trailing vortex.

Steady state computations were performed in this study to reduce the computational requirements of the research. Near the flap edge, a number of unsteady phenomena, such as separated flows, exist. Therefore a time-accurate investigation may be required to truly model the flow in this region. An unsteady analysis is certainly required to track any movement of the vortex core, which could influence the rest of the flowfield.

## REFERENCES

1. Meredith, P. T., "Viscous Phenomena Affecting High-Lift Systems And Suggestions For Future CFD Development," AGARD CP-515, Paper No. 19, Oct. 1992.
2. Butter, D. J., "Recent Progress on Development and Understanding of High Lift Systems," AGARD CP-365, Paper No. 1, Aug. 1984.
3. Brune, G. W. and McMasters, J. H., "Computational Aerodynamics Applied to High-Lift Systems," in *Applied Computational Aerodynamics*, P. A. Henne, ed., American Institute of Aeronautics and Astronautics, Washington, DC, 1990.
4. Flaig, A. and Hilbig, R., "High-Lift Design For Large Civil Aircraft," AGARD CP-515, Paper No. 31, Oct. 1992.
5. Smith, A. M. O., "High-Lift Aerodynamics," AIAA Paper 74-939, Aug. 1974.
6. Dillner, B., May, F. W., and McMasters, J. H., "Aerodynamic Issues in the Design of High-Lift Systems for Transport Aircraft," AGARD CP-365, Paper No. 9, Aug. 1984.
7. Woodward, D. S., Hardy, B. C., and Ashill, P. R., "Some Types of Scale Effects in Low-Speed, High-Lift Flows," 16<sup>th</sup> ICAS Congress, 1988.
8. Obert, E., "Forty Years Of High-Lift R & D - An Aircraft Manufacturer's Experience," AGARD CP-515, Paper No. 27, Oct. 1992.
9. Valarezo, W. O., Dominik, C. J., McGhee, R. J., Goodman, W. L., and Paschal, K. B., "Multi-Element Airfoil Optimization for Maximum Lift at High Reynolds Numbers," AIAA Paper 91-3332, Sept. 1991.
10. Valarezo, W. O., Dominik, C. J., McGhee, R. J., and Goodman, W. L., "High Reynolds Number Configuration Development of a High-Lift Airfoil," AGARD CP-515, Paper No. 10, Oct. 1992.
11. Valarezo, W. O., Dominik, C. J., and McGhee, R. J., "Reynolds and Mach Number Effects on Multielement Airfoils," in *Proceedings of the Fifth Numerical and Physical Aspects of Aerodynamic Flows*, California State University, Long Beach, CA, Jan. 1992.
12. Chin, V. D., Peters, D. W., Spaid, F. W., and McGhee, R. J., "Flowfield Measurements About A Multi-Element Airfoil At High Reynolds Numbers," AIAA Paper 93-3137, July 1993.

13. Ross, J. C., Storms, B. L., and Carrannanto, P. C., "Lift-Enhancing Tabs on Multi-Element Airfoils," AIAA Paper 93-3504, Aug. 1993.
14. Storms, B. L. and Ross, J. C., "An Experimental Study of Lift-Enhancing Tabs on a Two-Element Airfoil," AIAA Paper 94-1868, June 1994.
- ✓15. Olson, L. E., "Optimization of Multielement Airfoils for Maximum Lift," NASA CP-2045, Vol. 1, Mar. 1978, pp. 237-253.
16. Brune, G. W. and Manke, J. W., "Upgraded Viscous Flow Analysis Of Multielement Airfoils," NASA CP-2045, Vol. 1, Mar. 1978, pp. 163-181.
17. Hardin, J. D., Potter, R. C., van Dam, C. P., and Yip, L. P., "Two-Dimensional Computational Analysis Of A Transport High-Lift System And Comparison With Flight-Test Results," AIAA Paper 93-3533, Aug. 1993.
18. Jacob, K., "A Fast Computing Method For The Flow Over High-Lift Wings," AGARD CP-515, Paper No. 23, Oct. 1992.
19. Drela, M., "A User's Guide to MSES V1.2," MIT Computational Fluid Dynamics Laboratory, July 1991.
20. Rogers, S. E., "Efficient Simulation of Incompressible Viscous Flow Over Single and Multi-Element Airfoils," AIAA Paper 92-0405, Jan. 1992.
21. Rogers, S. E., "Progress in High-Lift Aerodynamic Calculations," AIAA Paper 93-0194, Jan. 1993.
22. Rogers, S. E., Menter, F. R., Durbin, P. A., Mansour, N. N., "A Comparison Of Turbulence Models In Computing Multi-Element Airfoils Flows," AIAA Paper 94-0291, Jan. 1994.
23. Carrannanto, P. C., Storms, B. L., Ross, J. C., and Cummings, R. M., "Navier-Stokes Analysis of Lift-Enhancing Tabs on Multi-Element Airfoils," AIAA Paper 94-0050, Jan. 1994.
24. Mani, M. and Bush, R. H., "Overlapping Grid Method for High-Lift and Store Carriage Applications," AIAA Paper 93-3428, Aug. 1993.
25. Nelson, T. E., Zingg, D. W., and Johnston, G. W., "Numerical Solution of the Navier-Stokes Equations for High-Lift Configurations on Structured Composite Grids," AGARD CP-515, Paper No. 9, Oct. 1992.
26. Jasper, D., Agrawal, S., and Robinson, B. A., "Navier-Stokes Calculations on Multi-Element Airfoils Using A Chimera Based Solver," AGARD CP-515, Paper No. 8, Oct. 1992.

27. de Cock, K. M. J., "High-Lift System Analysis Using Unstructured Meshes," AGARD CP-515, Paper No. 12, Oct. 1992.
28. Davis, W. H. and Matus, R. J., "High Lift Multiple Element Airfoil Analysis with Unstructured Grids," AIAA Paper 93-3478, Aug. 1993.
29. Savory, E. Toy, N., Tahouri, B., and Dalley, S., "Flow Regimes in the Cove Regions Between a Slat and Wing and Between a Wing and Flap of a Multielement Airfoil," *Experimental Thermal and Fluid Science*, Vol. 5, No. 3, May 1992, pp. 307-316.
30. Horton, H. P., "Fundamental Aspects Of Flow Separation Under High-Lift Conditions," von Karman Institute for Fluid Dynamics, Brussels, Belgium, 1970.
31. van Dam, C. P., Vijgen, P. M. H. W., Yip, L. P., and Potter, R. C., "Leading Edge Transition And Relaminarization Phenomena On A Subsonic High-Lift System," AIAA Paper 93-3140, July 1993.
32. Earnshaw, P. B., Green, A. R., Hardy, B. C., and Jelly, A. H., "A Study Of The Use Of Half-Models In High-Lift Wind-Tunnel Testing," AGARD CP-515, Paper No. 20, Oct. 1992.
33. Bertin, J. J., *Engineering Fluid Mechanics*, Prentice Hall, Inc., New Jersey, 1987.
34. Anderson, D. A., Tannehill, J. C., and Pletcher, R. H., *Computational Fluid Mechanics and Heat Transfer*, Hemisphere Publishing Corp., New York, 1984.
35. Rogers, S. E., "Numerical Solution of the Incompressible Navier-Stokes Equations," NASA TM 102199, Nov. 1990.
36. Vinokur, M., "Conservation Equations of Gas-Dynamics in Curvilinear Coordinate Systems," *Journal of Computational Physics* Vol. 14, No. 2, Feb. 1974, pp. 105-125.
37. Baldwin B. S. and Barth, T. J., "A One-Equation Turbulent Transport Model for High Reynolds Wall Bounded Flows," AIAA Paper 91-0160, Jan. 1991.
38. Baldwin, B. S. and Lomax, H., "Thin Layer Approximation and Algebraic Model for Separated Turbulent Flows," AIAA Paper 78-257, Jan. 1978.
39. Mansour, N. N., Kim, J., and Moin, P., "Near-Wall  $k - \epsilon$  Turbulence Modeling," *AIAA Journal*, Vol. 27, No. 8, Aug. 1989, pp. 1068-1073.

40. Chorin, A. J., "A Numerical Method for Solving Incompressible Viscous Flow Problems," *Journal of Computational Physics*, Vol. 2, No. 1, Aug. 1967, pp. 12-26.
41. Roe, P. L., "Approximate Riemann Solvers, Parameter Vectors, and Difference Schemes," *Journal of Computational Physics*, Vol. 43, No. 2, Oct. 1981, pp. 357-372.
42. MacCormack, R. W., "Current Status of Numerical Solutions of the Navier-Stokes Equations," AIAA Paper 85-0032, Jan. 1985.
43. Hicks, R. M. and Schairer E. T., "Effects of Upper Surface Modification on the Aerodynamic Characteristics of the NACA 632-215 Airfoil Section," NASA TM 78503, 1979.
44. Chan, W. M., Ing-Tsau, C., and Buning, P. G., "User's Manual for the HYPGEN Hyperbolic Grid Generator and the HGUI Graphical User Interface," NASA TM 108791, Oct. 1993.
45. Tramel, T. W. and Suhs, J. L., "PEGSUS 4.0 User's Manual," AEDC TR-91-8, June 1991.
46. Benek, J. A., Buning, P. G., and Steger, J. L., "A 3-D Chimera Grid Embedding Technique," AIAA Paper 85-1523, July 1985.
47. Ashby, D. L., personal communication, Feb. 1994.
48. Ashby, D. L., Dudley, M. R., Iguchi, S. K., Browne, L., and Katz, J., "Potential Flow Theory and Operation Guide for the Panel Code PMARC," NASA TM 102851, Jan. 1991.

Type	B-47/B-52	367-80/ KC-135	707-320/ E-3A	727	747/E-4A	767
First flight	1947/1952	1954	1962	1963	1969	1981
Planform						
Typical airfoil						
	Single-slotted fowler flap	Double- slotted flap	Double slotted flap and Krueger leading edge	Slat and triple-slotted flap	Variable camber Krueger and triple-slotted flap	Slat and single-slotted flap
$C_{L_{max}}$	1.8	1.78	2.2	2.79	2.45	2.45

Figure 1: Trends in Boeing transport high-lift system development (from Reference 3).

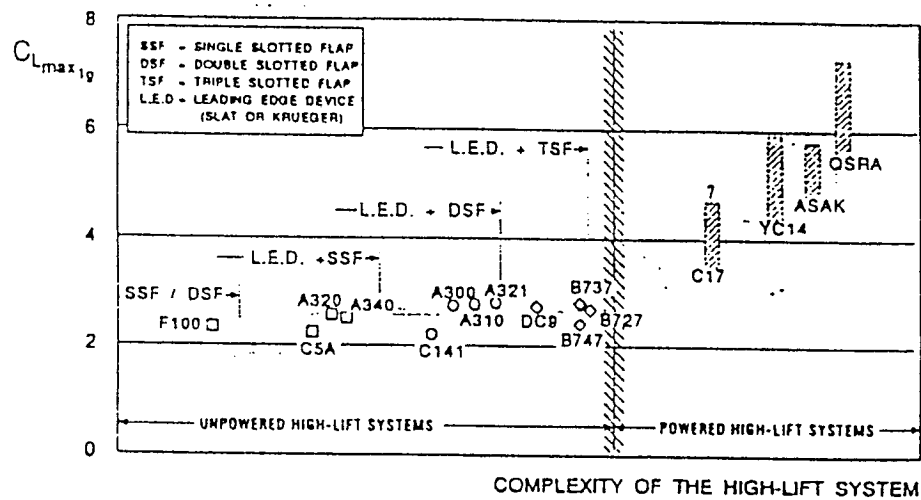


Figure 2: Lift efficiency versus high-lift system complexity (from Reference 4).

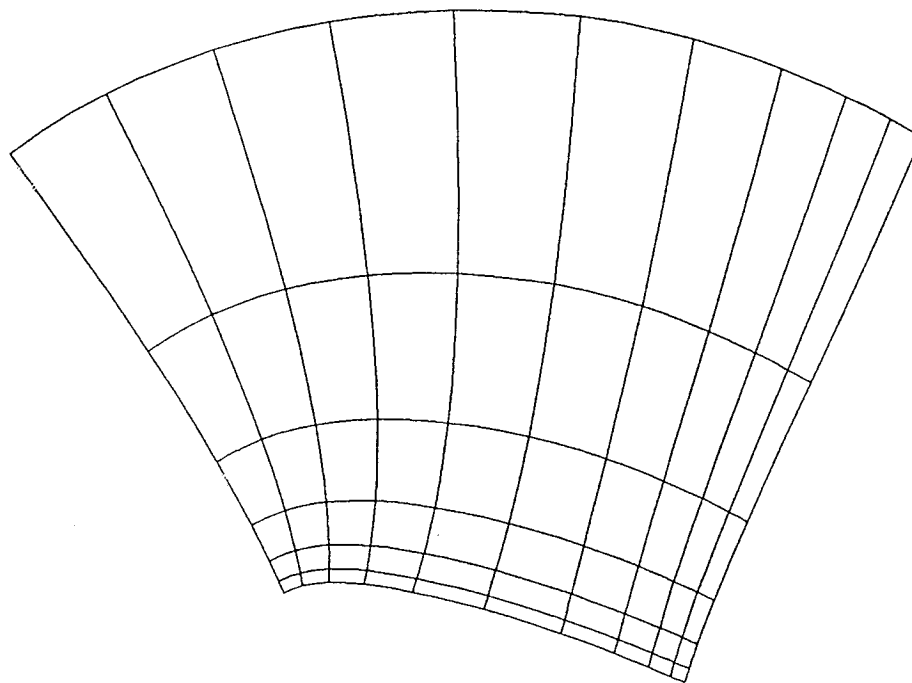


Figure 3: Curved computational mesh.

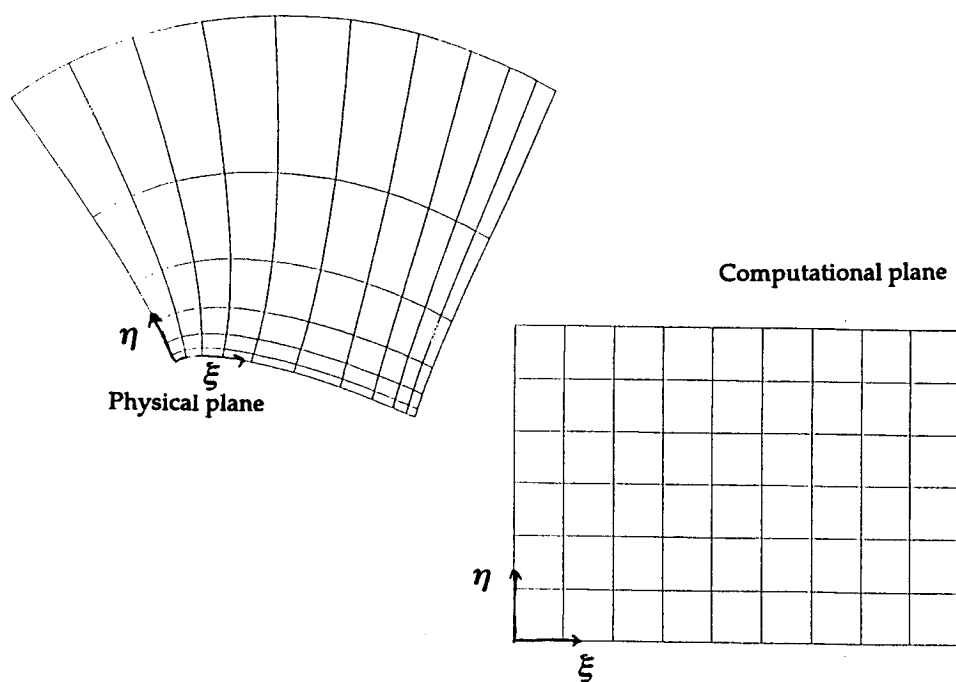


Figure 4: Relationship between physical and computational domains.



Figure 5: NACA 632-215 Mod. B airfoil.



Figure 6: NACA 632-215 Mod. B airfoil with 30% chord Fowler flap in take-off configuration.



Figure 7: NACA 632-215 Mod. B airfoil with 30% chord Fowler flap in landing configuration.

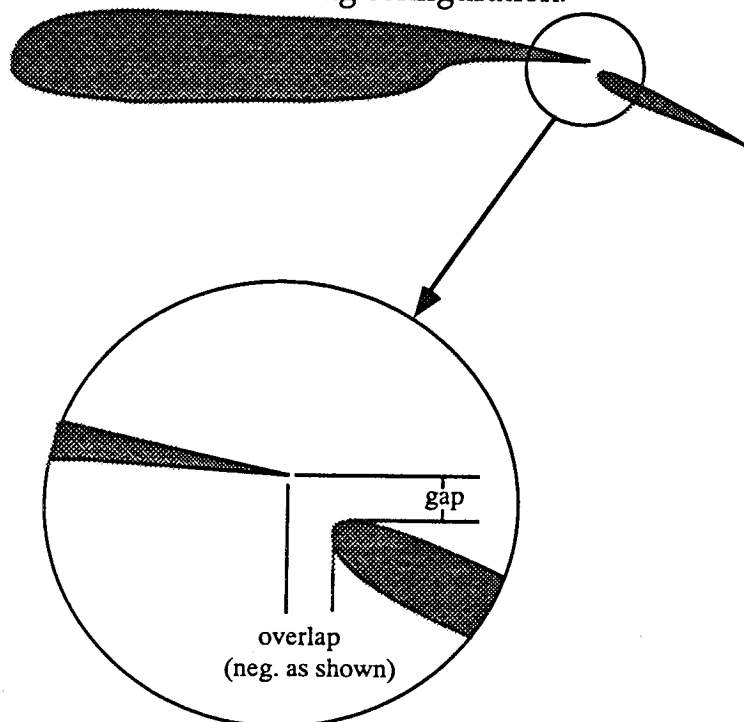


Figure 8: Definition of gap and overlap.

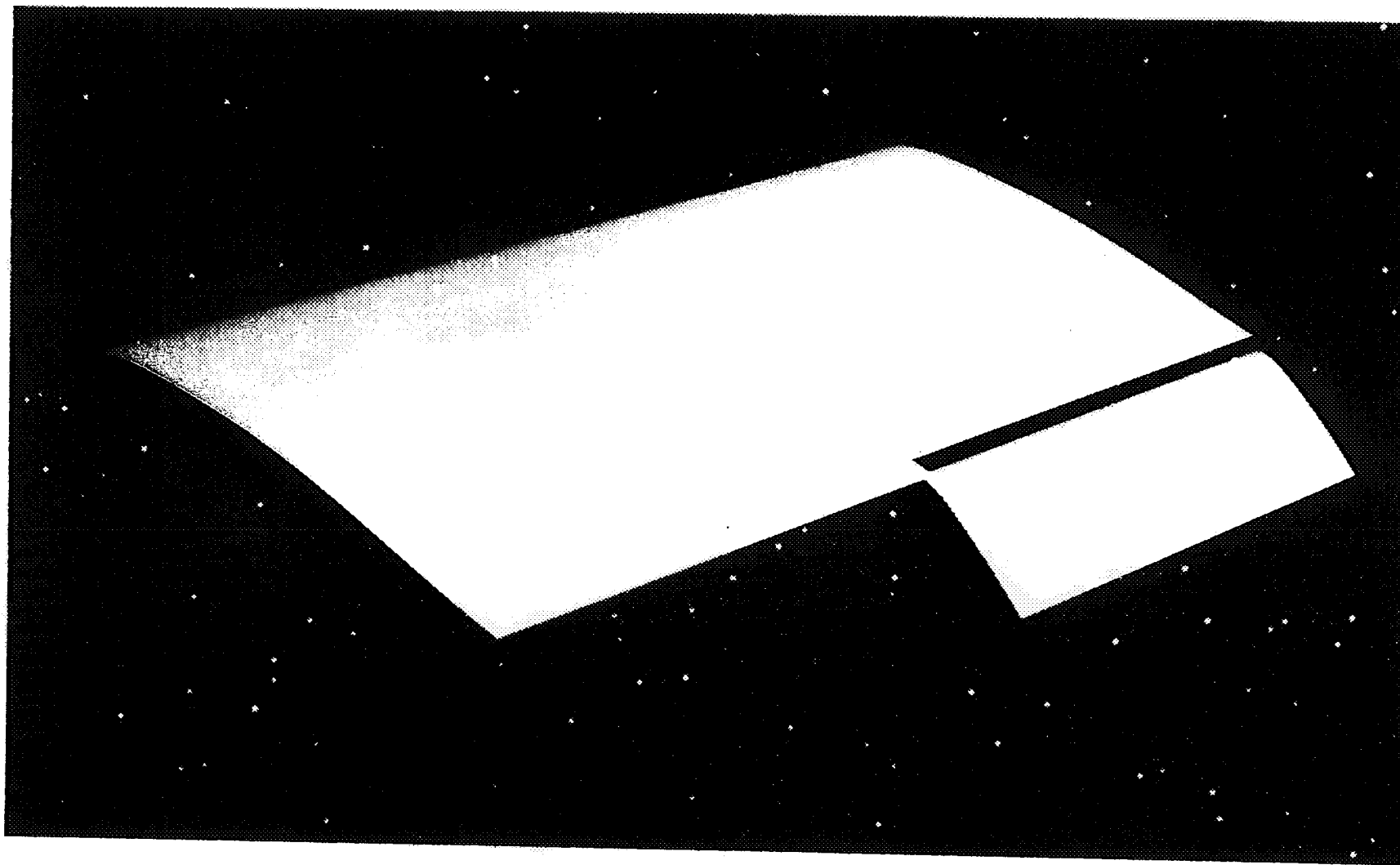


Figure 9: Half-span flap geometry.

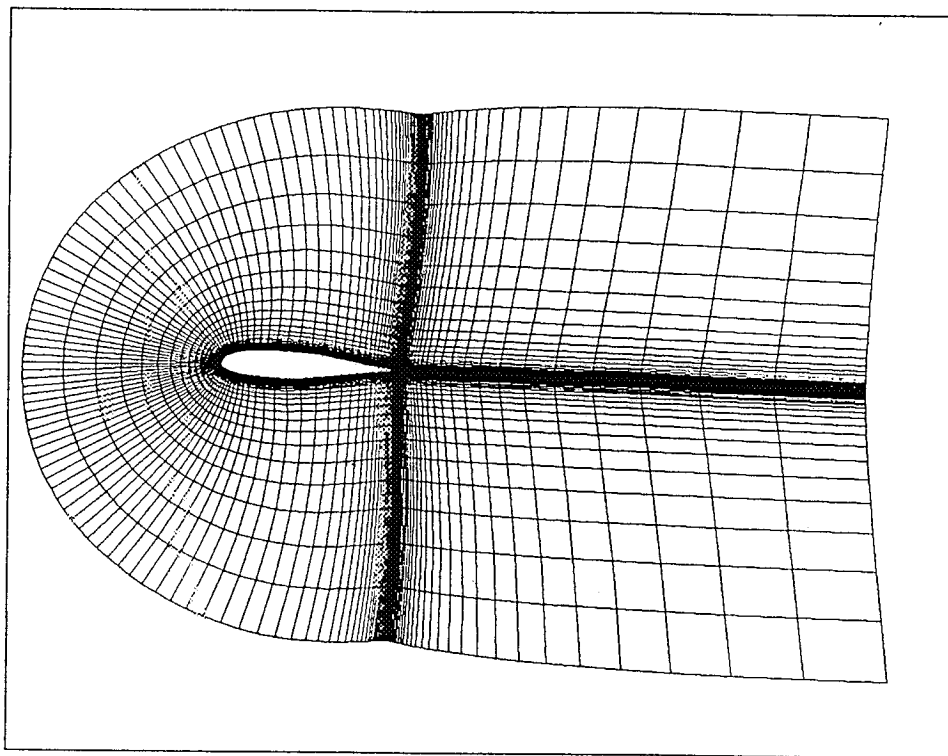


Figure 10: A two-dimensional grid plane.

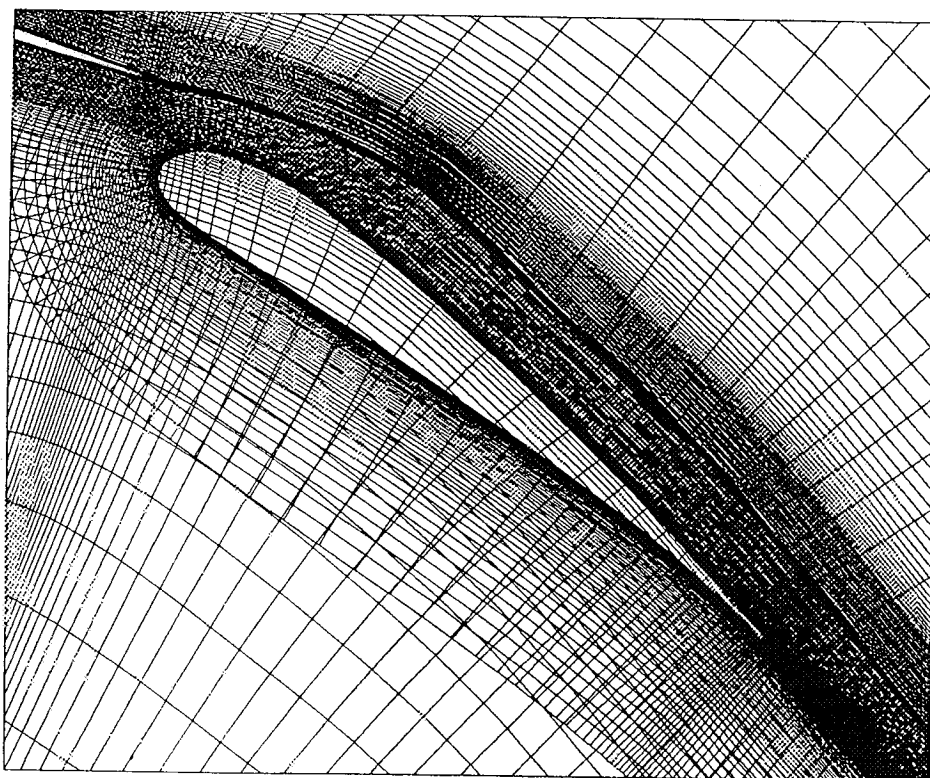


Figure 11: Overset grids before removing points inside flap surface.

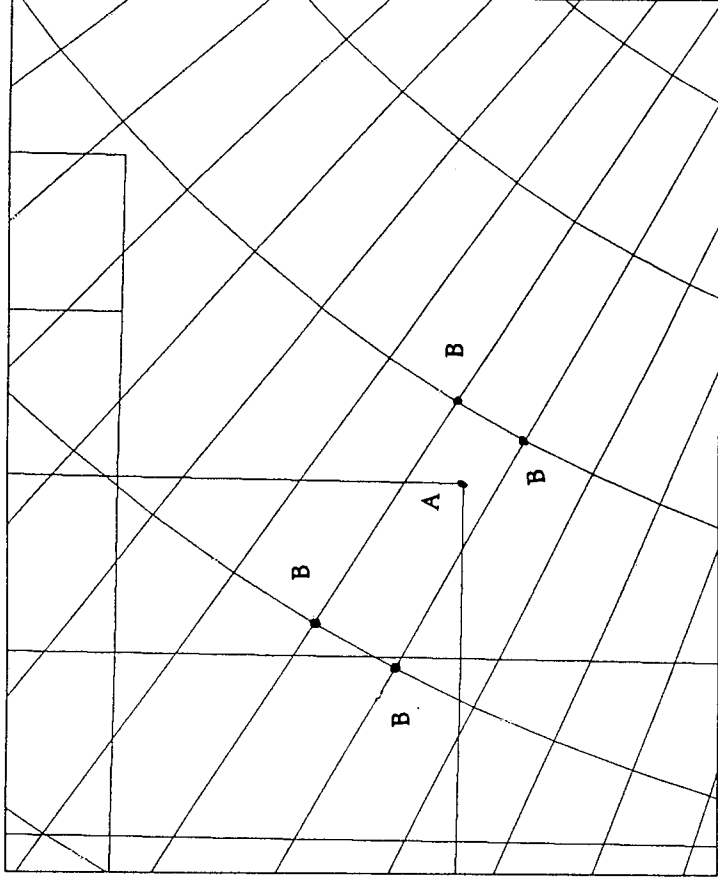


Figure 12: Chimera interpolation stencil.

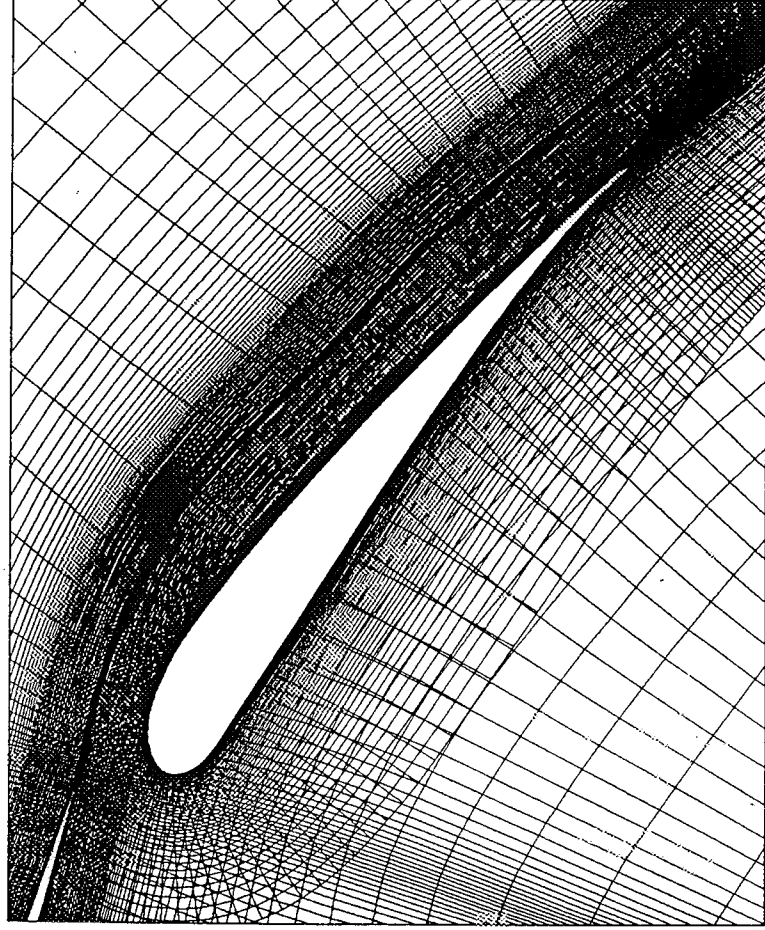


Figure 13: Use of hole-cuts to create overset grids.

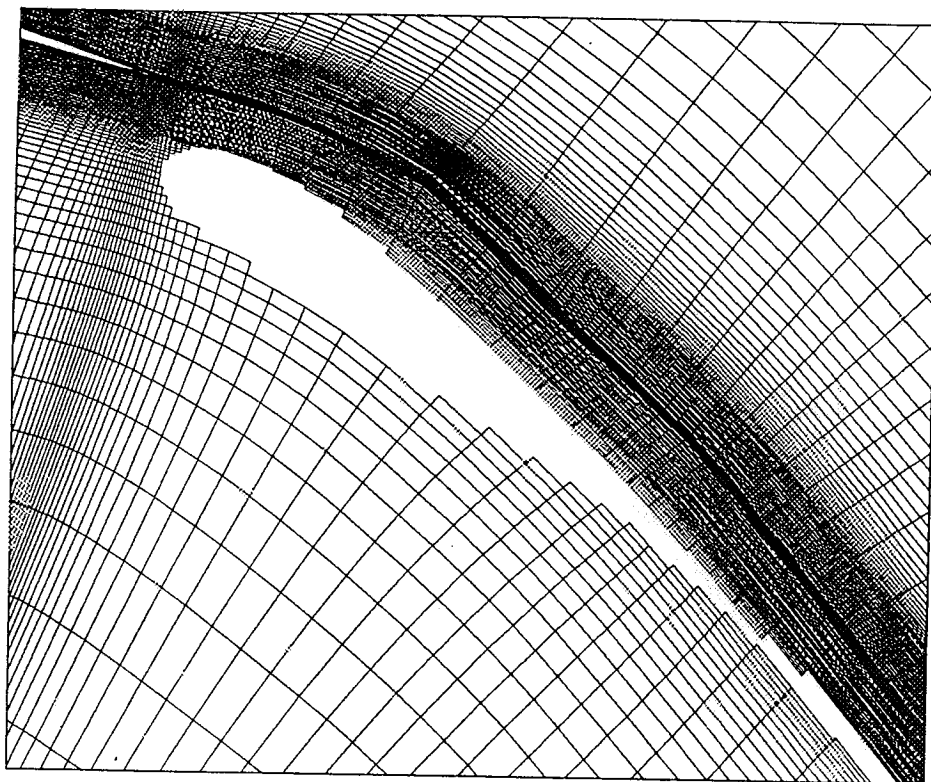


Figure 14: Hole-cut in a computational mesh.

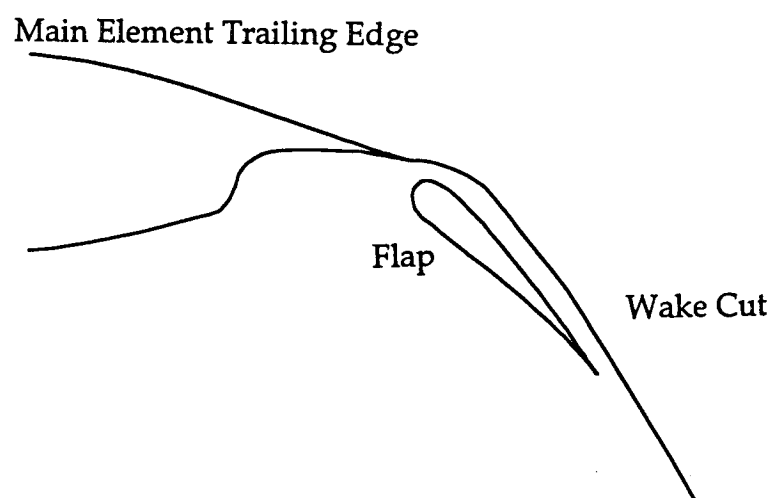


Figure 15: Main element wake cut placement.

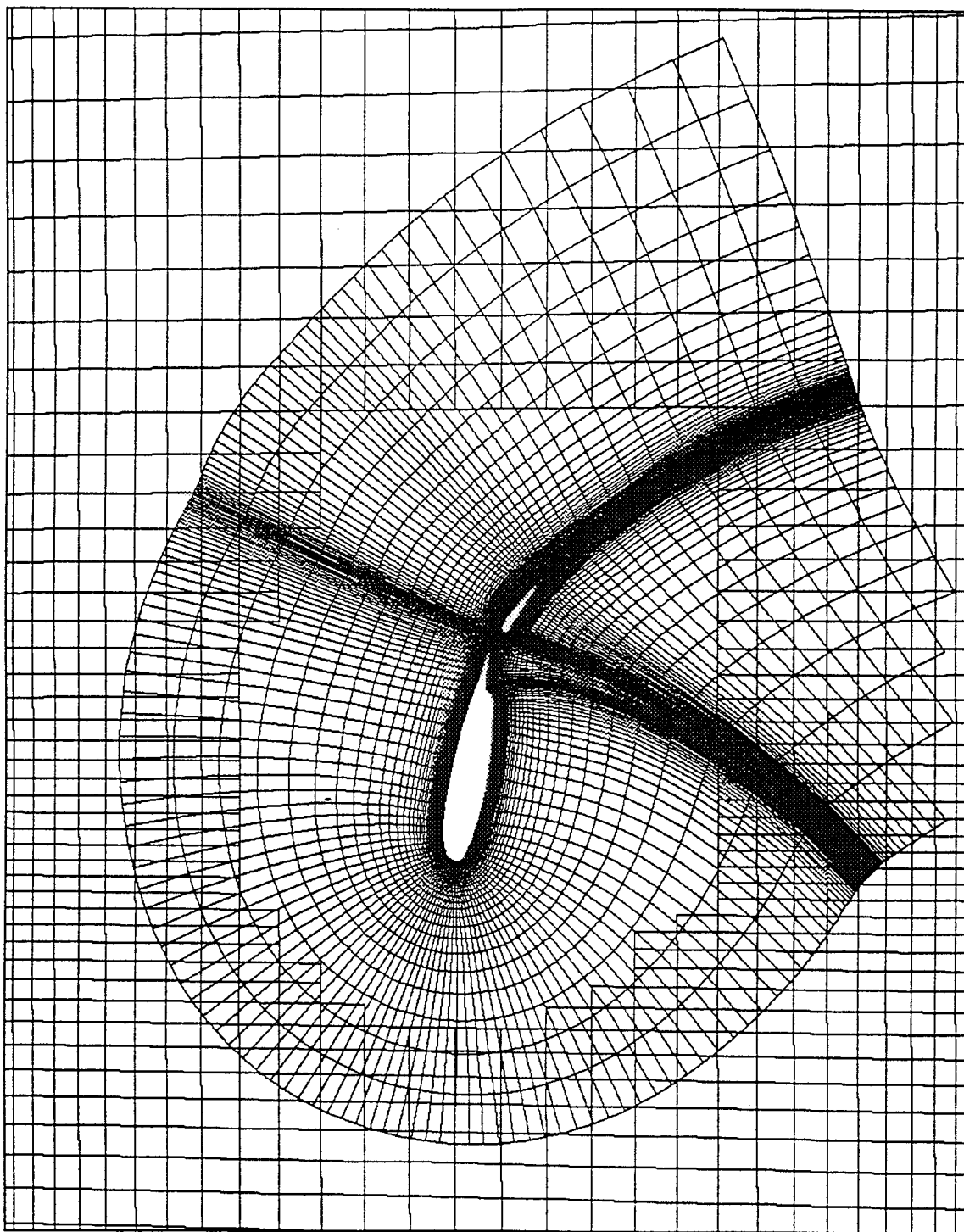


Figure 16: Landing configuration airfoil grid.

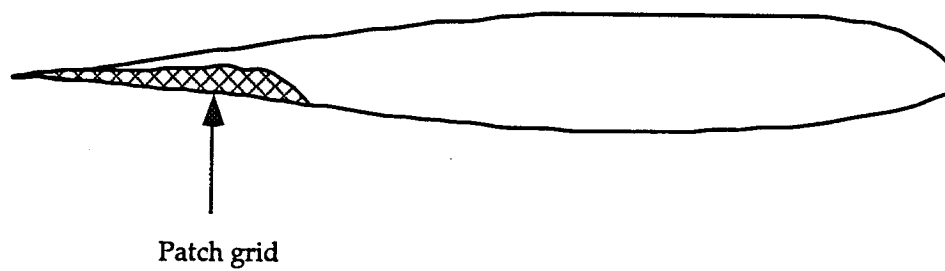


Figure 17: Exposed surface at flapped-unflapped intersection.

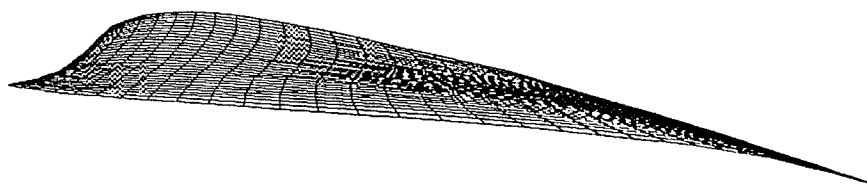


Figure 18: Patch grid plane.

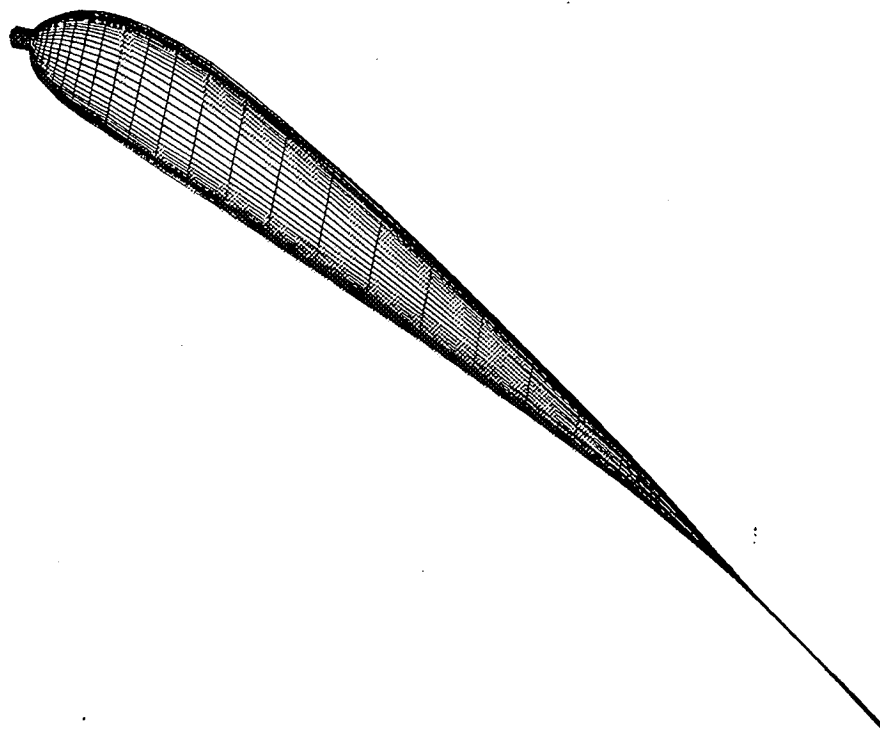


Figure 19: Flap edge grid plane.

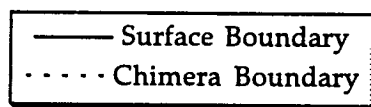


Figure 20: Boundary conditions at flapped-unflapped intersection.

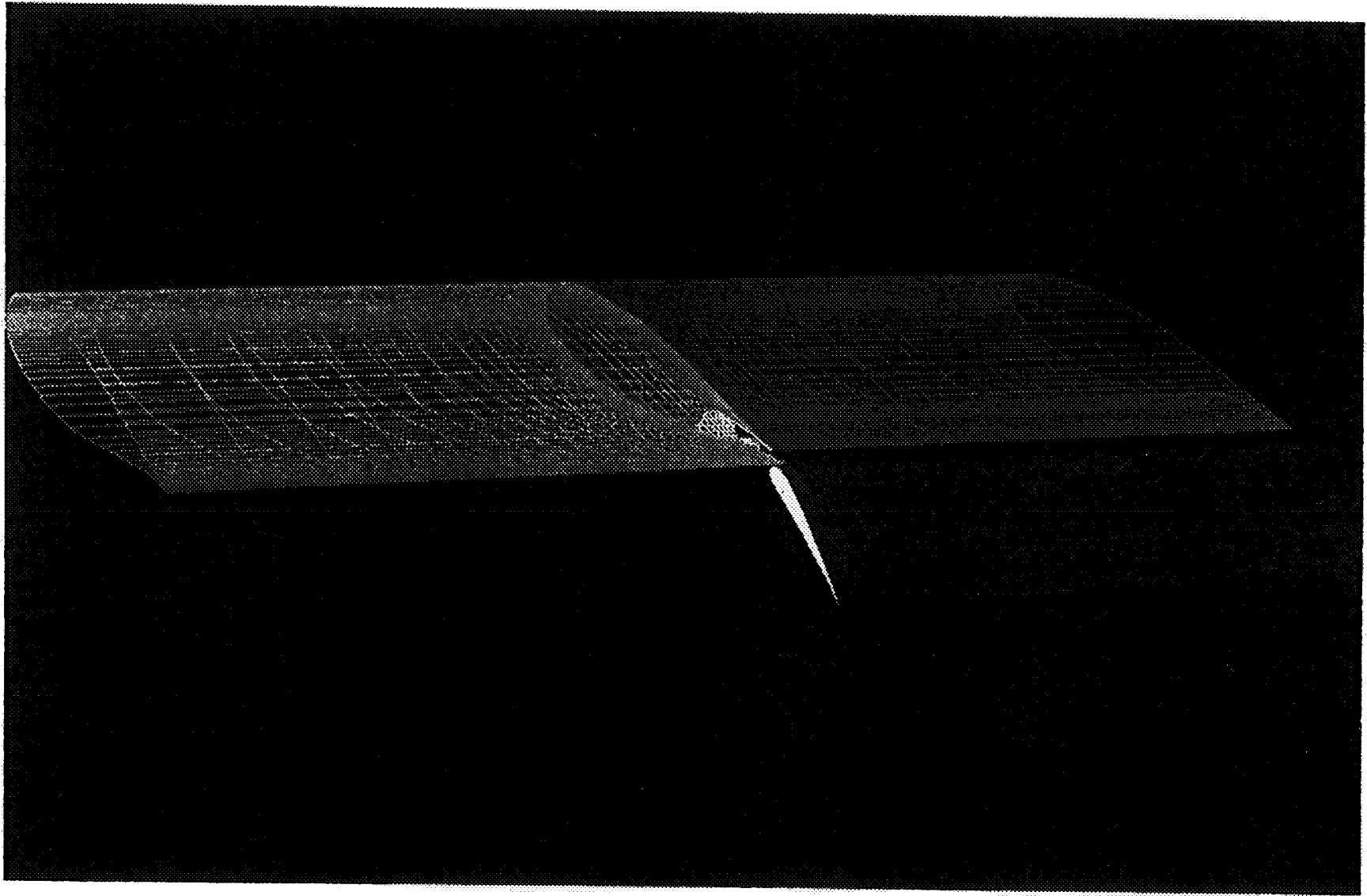


Figure 21: Half-span flap surface grid.

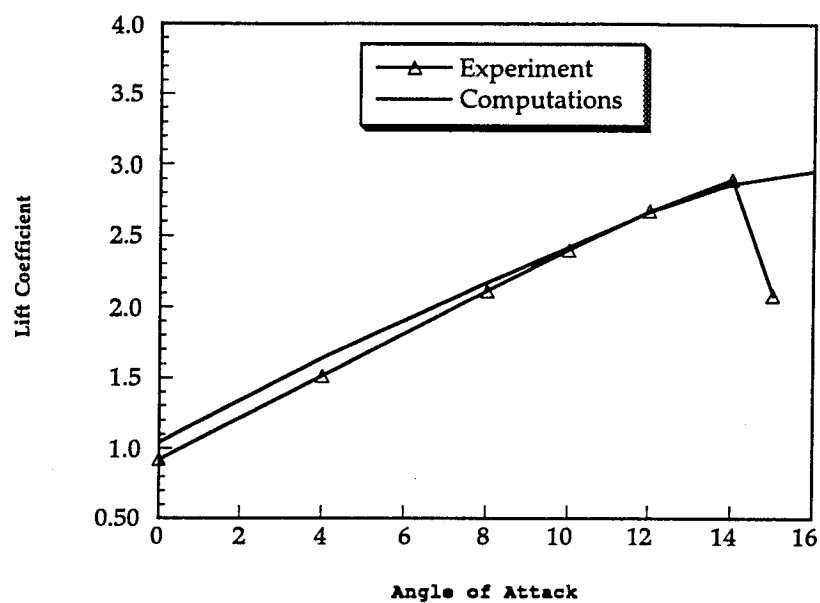


Figure 22: Lift coefficient versus angle of attack for two-dimensional take-off configuration.

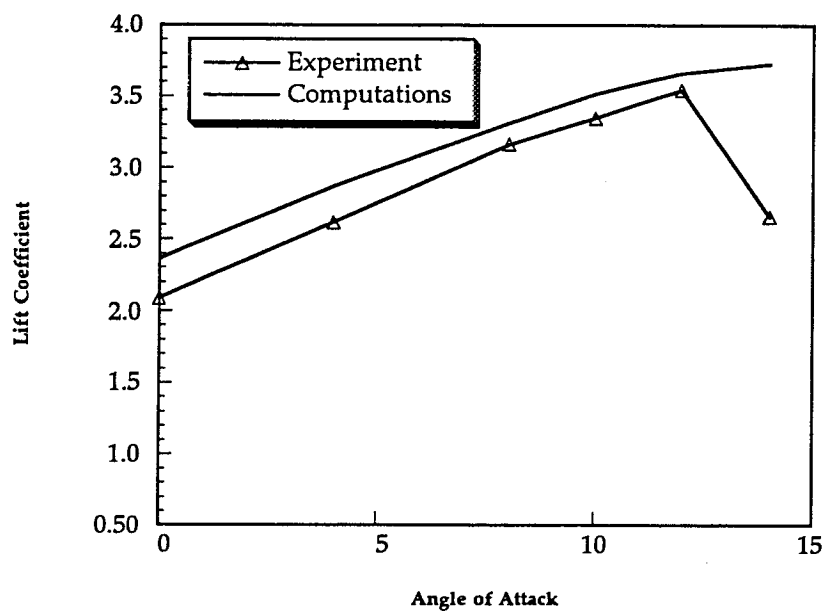


Figure 23: Lift coefficient versus angle of attack for two-dimensional landing configuration.

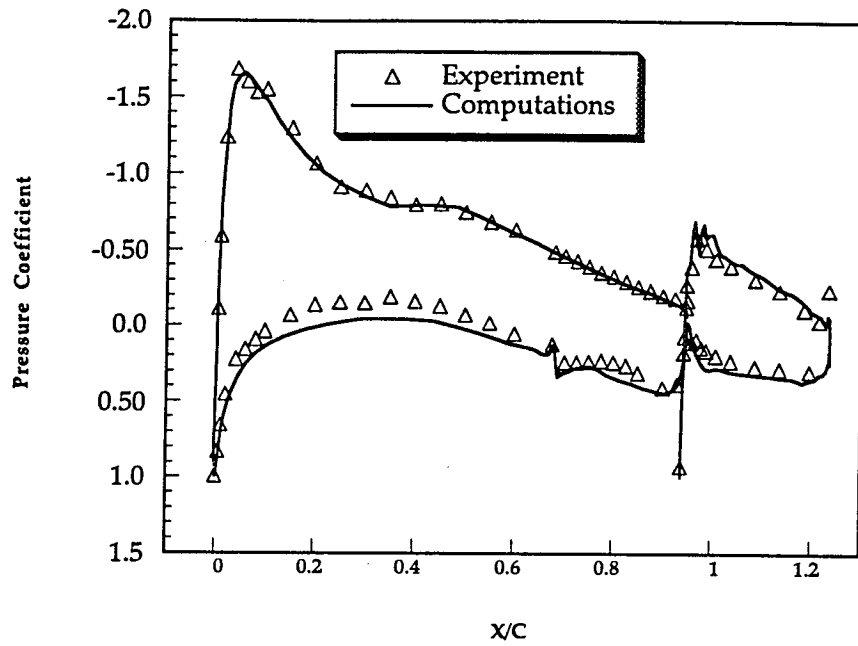


Figure 24: Pressure distribution for two-dimensional take-off configuration,  $\alpha=0^\circ$ .

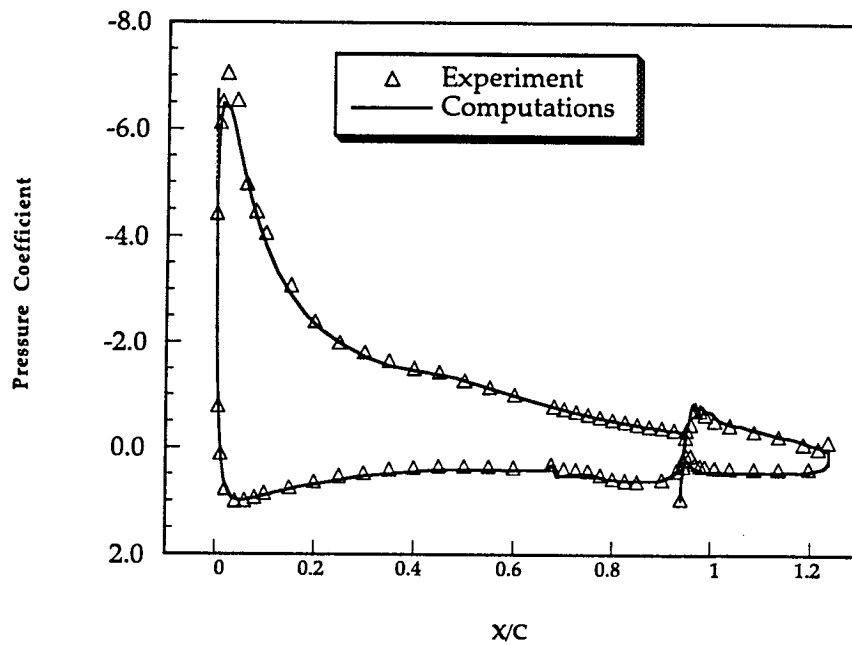


Figure 25: Pressure distribution for two-dimensional take-off configuration,  $\alpha=10^\circ$ .

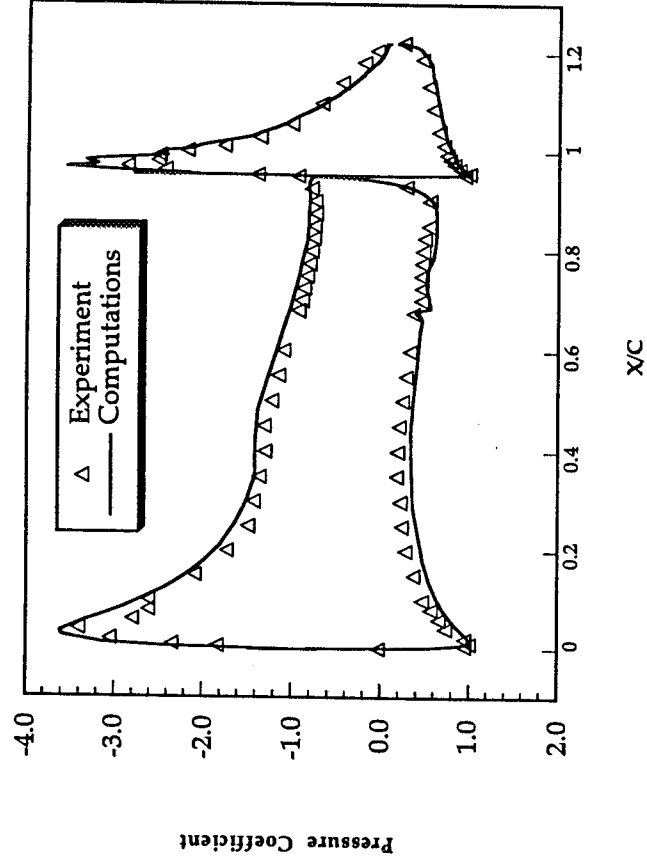


Figure 26: Pressure distribution for two-dimensional landing configuration,  $\alpha = 0^\circ$ .

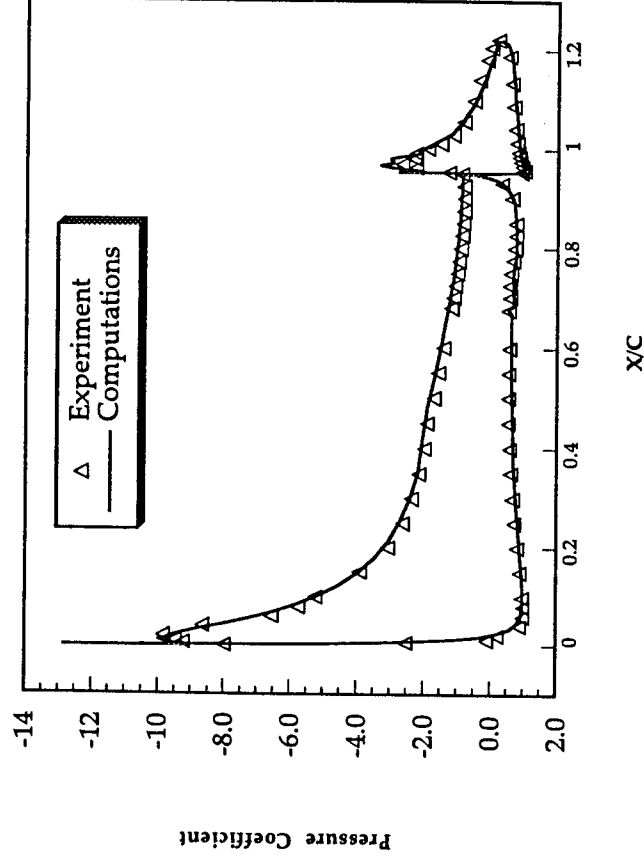


Figure 27: Pressure distribution for two-dimensional landing configuration,  $\alpha = 10^\circ$ .

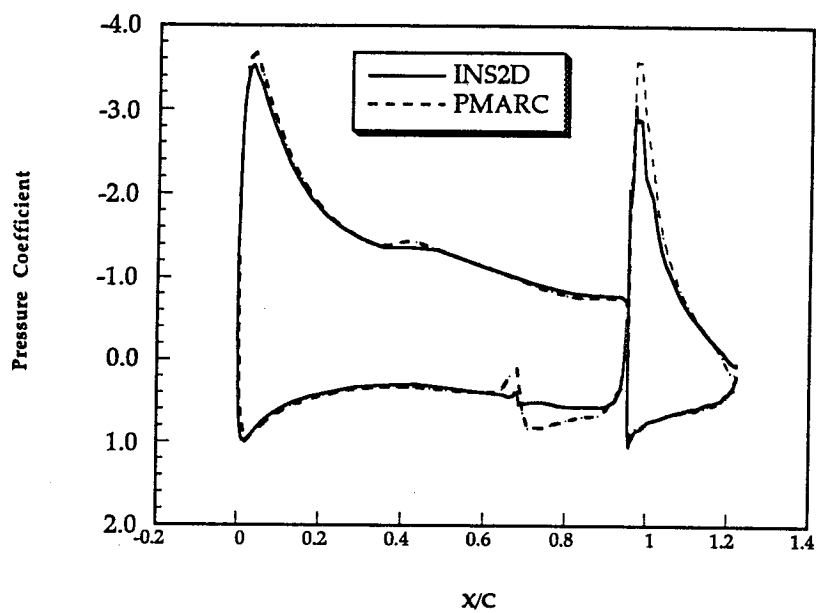


Figure 28: Pressure distribution for two-dimensional landing configuration without wind tunnel walls,  $\alpha = 0^\circ$ .

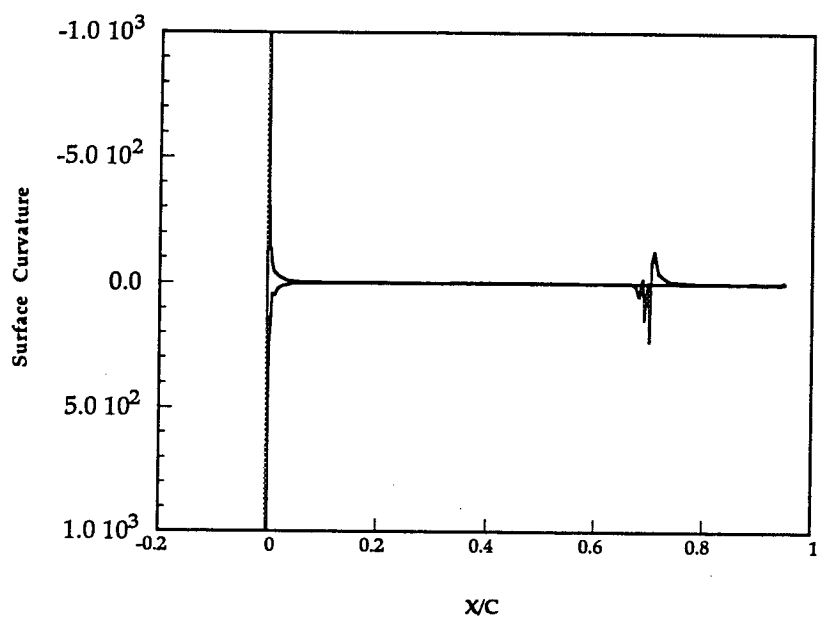


Figure 29: Surface curvature for flapped main element.

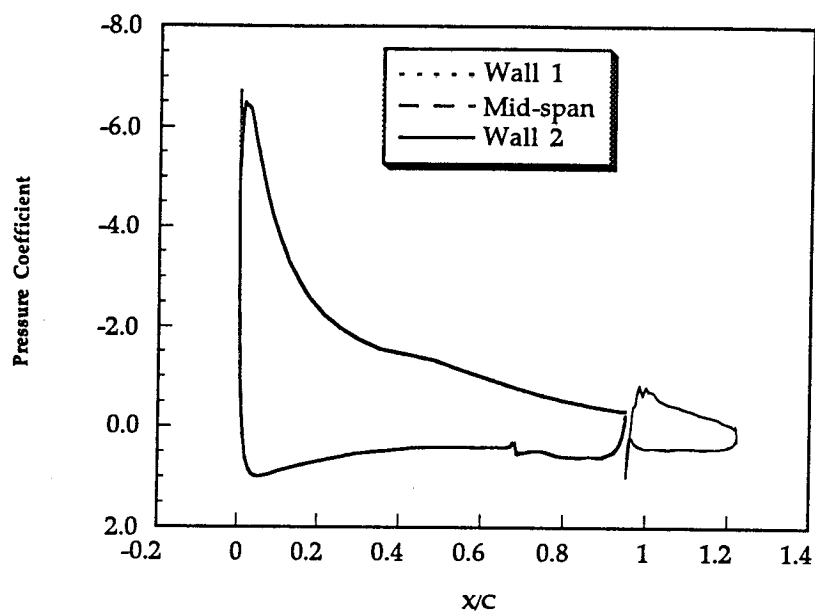


Figure 30: Pressure distributions for three spanwise stations on full-span flap,  $\alpha=10^\circ$ .

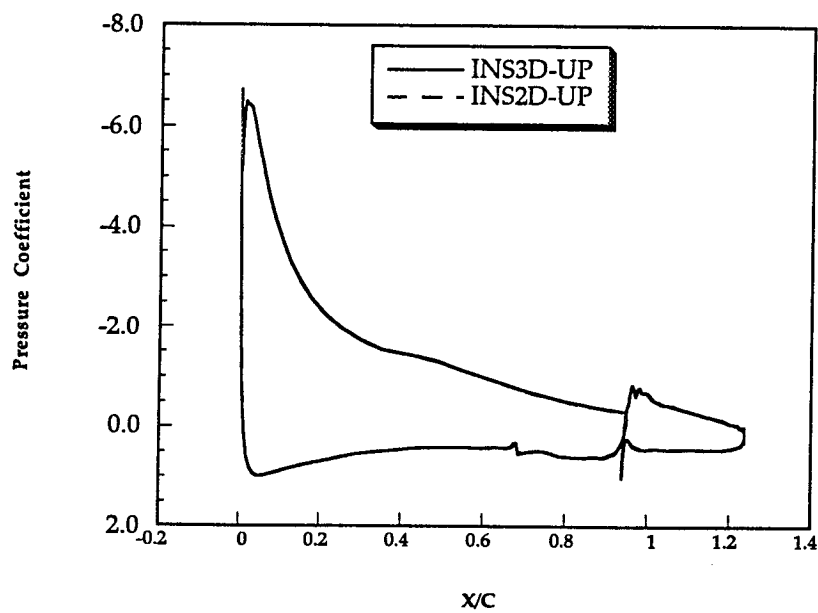


Figure 31: Pressure distributions computed with INS2D-UP and INS3D-UP for full-span flap,  $\alpha=10^\circ$ .

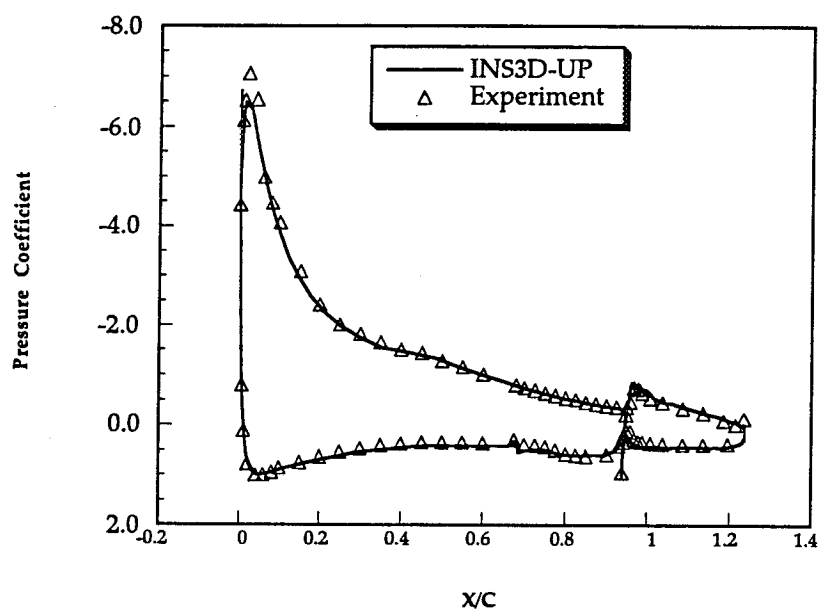


Figure 32: Experimental and computational full-span flap pressure distributions,  $\alpha=10^\circ$ .

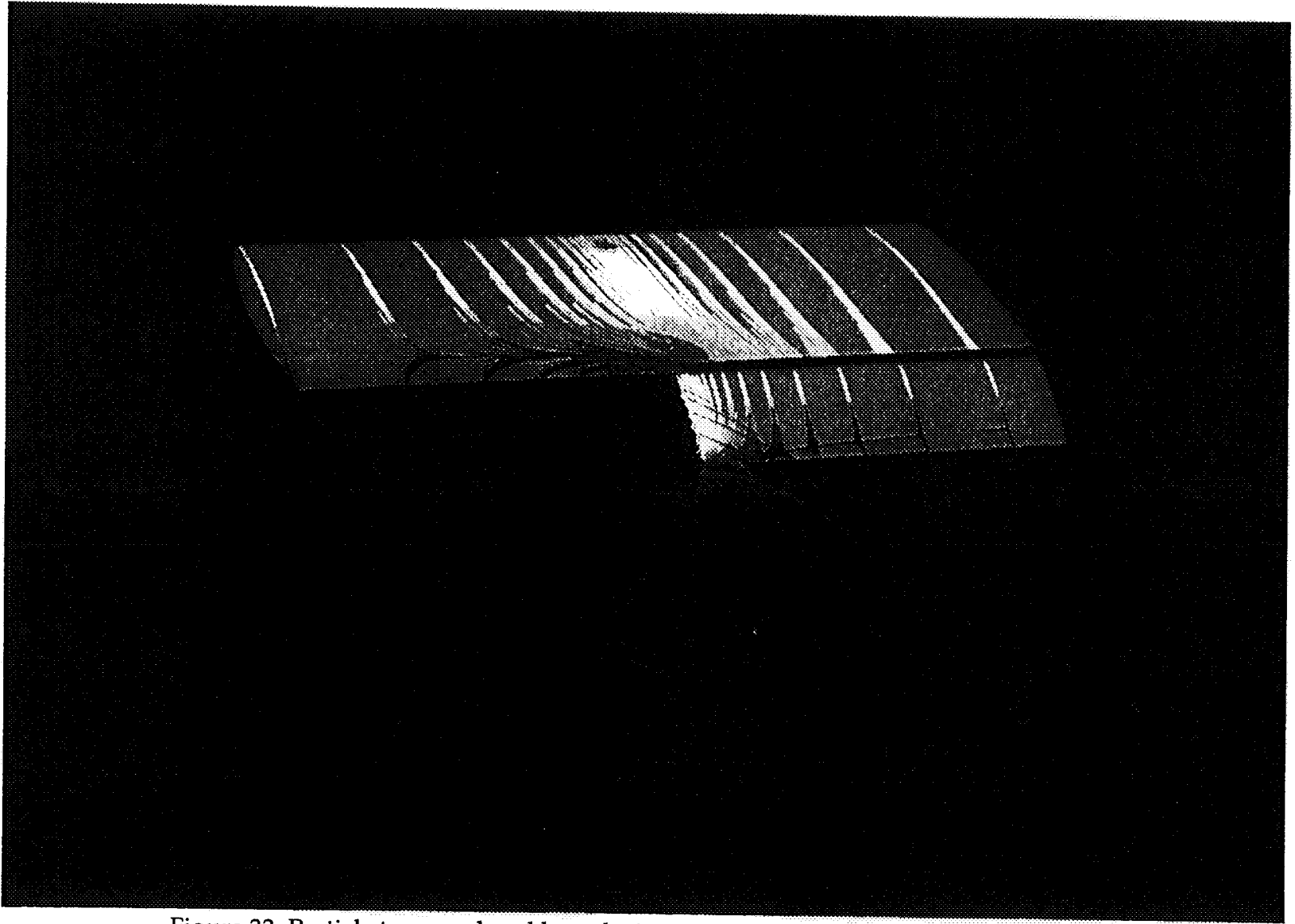


Figure 33: Particle traces colored by velocity magnitude for half-span flap in landing configuration,  $\alpha=10^\circ$ .

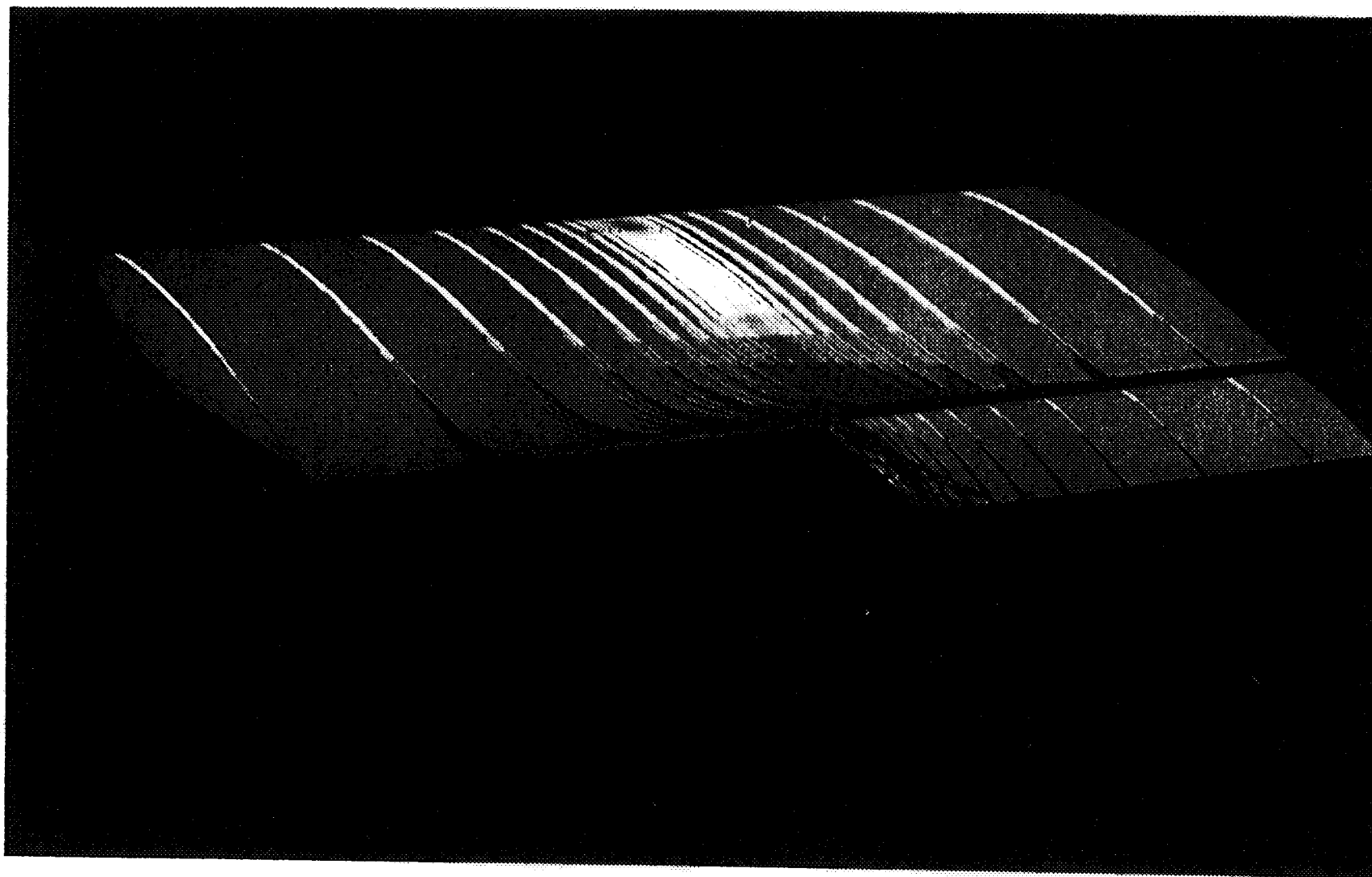


Figure 34: Particle traces colored by velocity magnitude for half-span flap in take-off configuration,  $\alpha = 10^\circ$ .

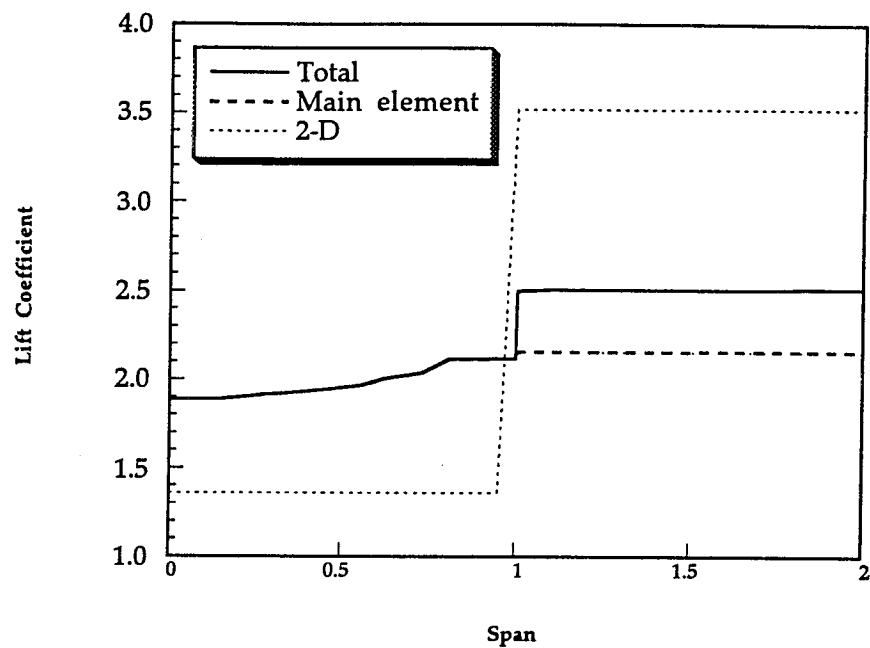


Figure 35: Lift-distribution for landing case,  $\alpha=10^\circ$ .

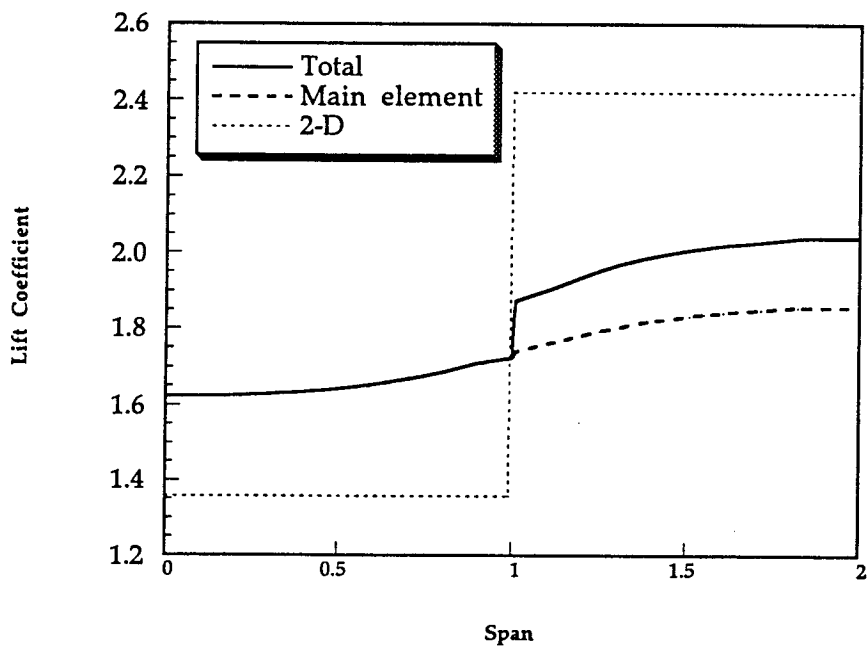


Figure 36: Lift-distribution for take-off case,  $\alpha=10^\circ$ .

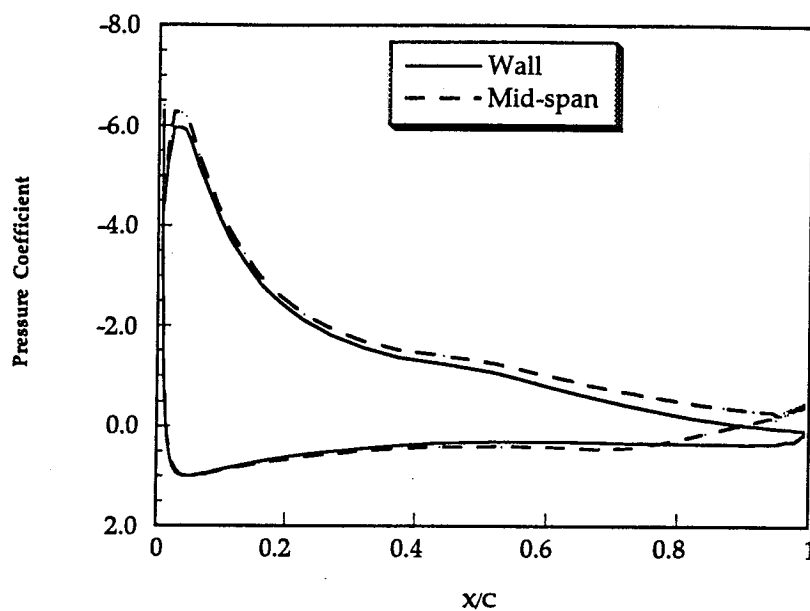


Figure 37: Spanwise pressure variation for landing configuration unflapped main element,  $\alpha = 10^\circ$ .

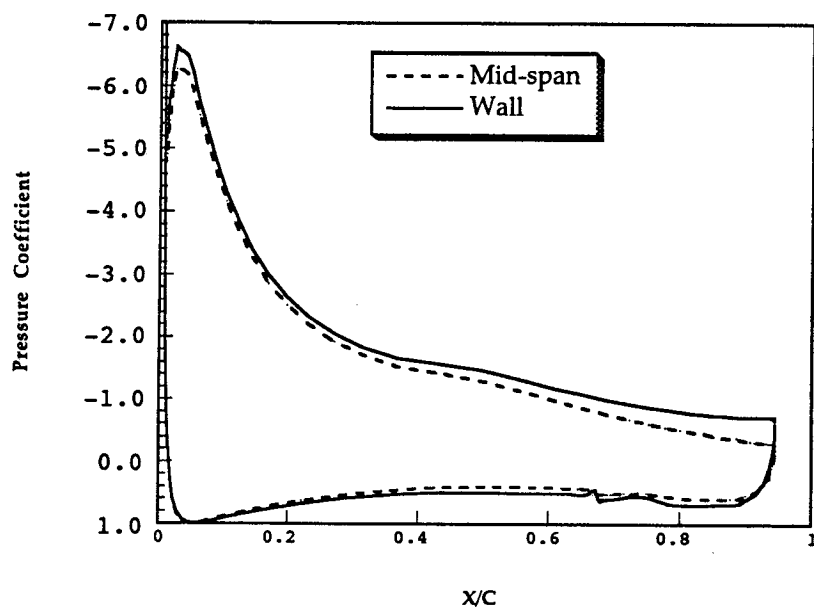


Figure 38: Spanwise pressure variation for landing configuration flapped main element,  $\alpha = 10^\circ$ .

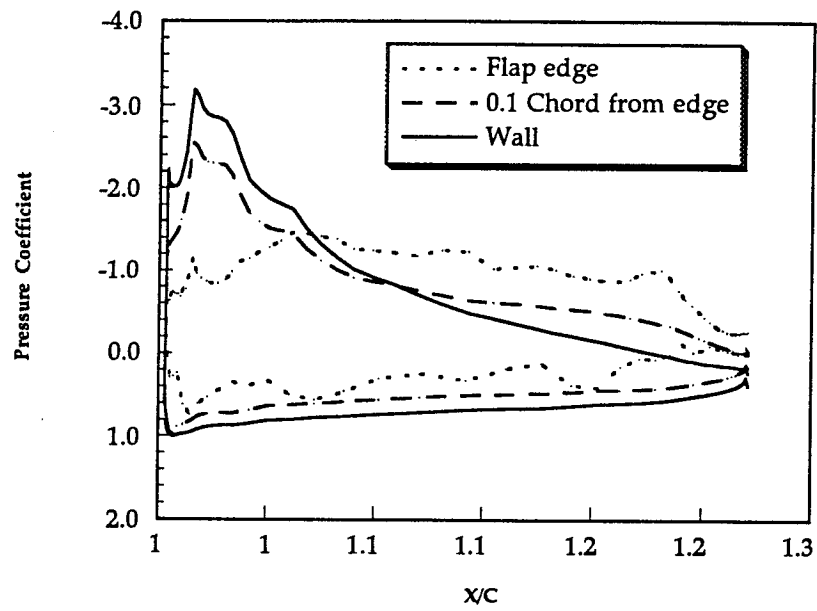


Figure 39: Spanwise pressure variation for landing configuration flap element,  $\alpha = 10^\circ$ .



Figure 40: Flap surface particle traces for landing configuration.

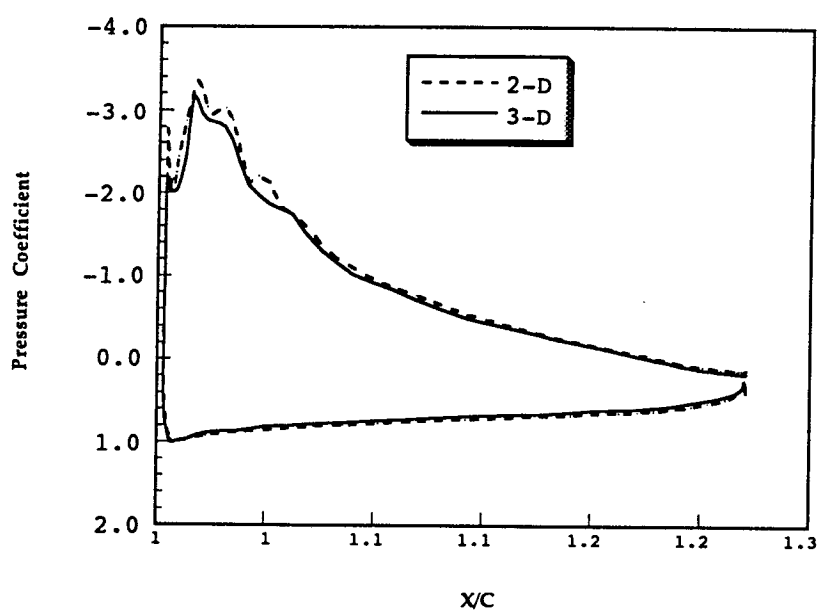


Figure 41: Pressure distribution comparison between half-span and airfoil computations for landing configuration flap element,  $\alpha=10^\circ$ .

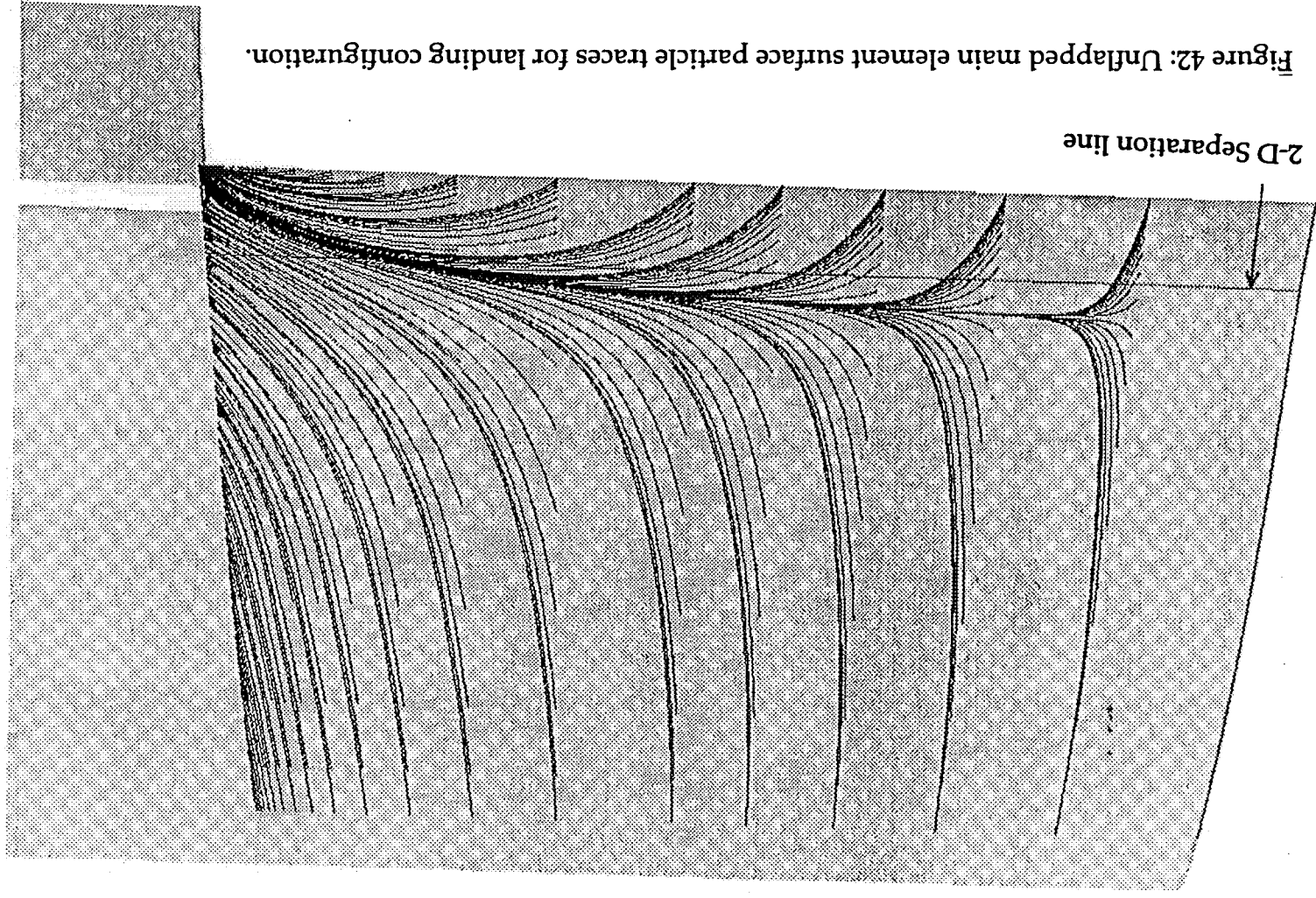


Figure 42: Unflapped main element surface particle traces for landing configuration.

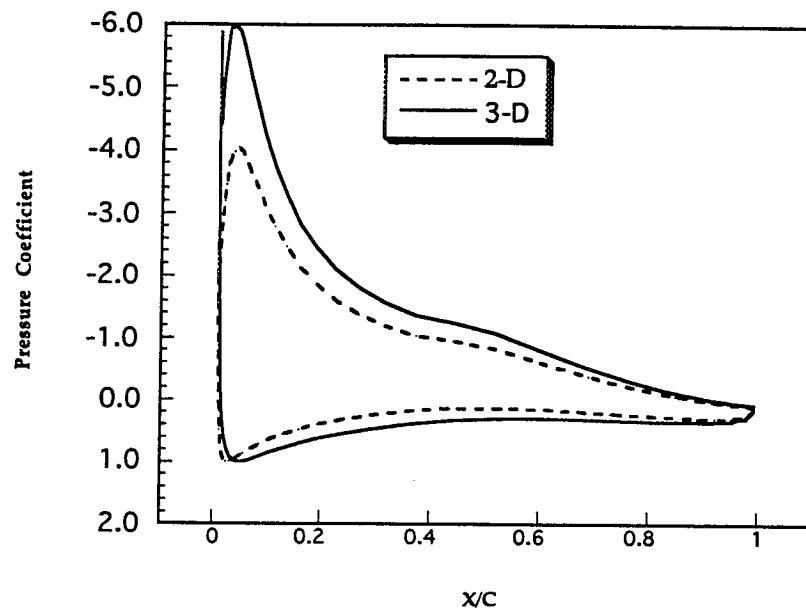


Figure 43: Pressure distribution comparison between half-span and airfoil computations for landing configuration unflapped element,  $\alpha=10^\circ$ .

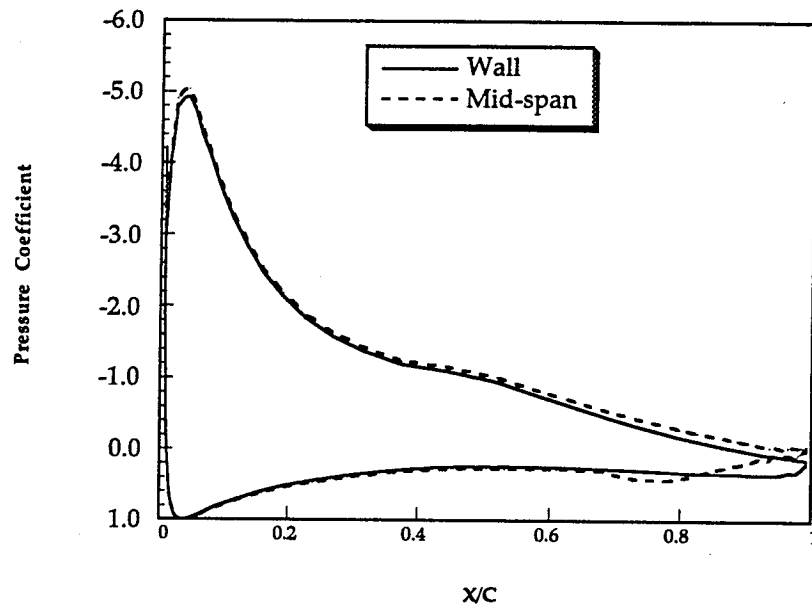


Figure 44: Spanwise pressure variation for landing configuration unflapped main element,  $\alpha=10^\circ$ .

C-2

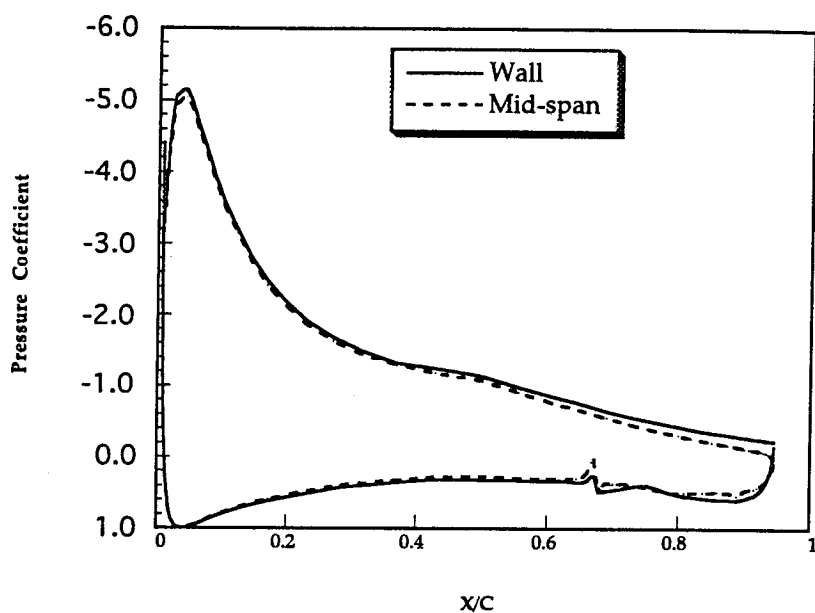


Figure 45: Spanwise pressure variation for landing configuration flapped main element,  $\alpha = 10^\circ$ .

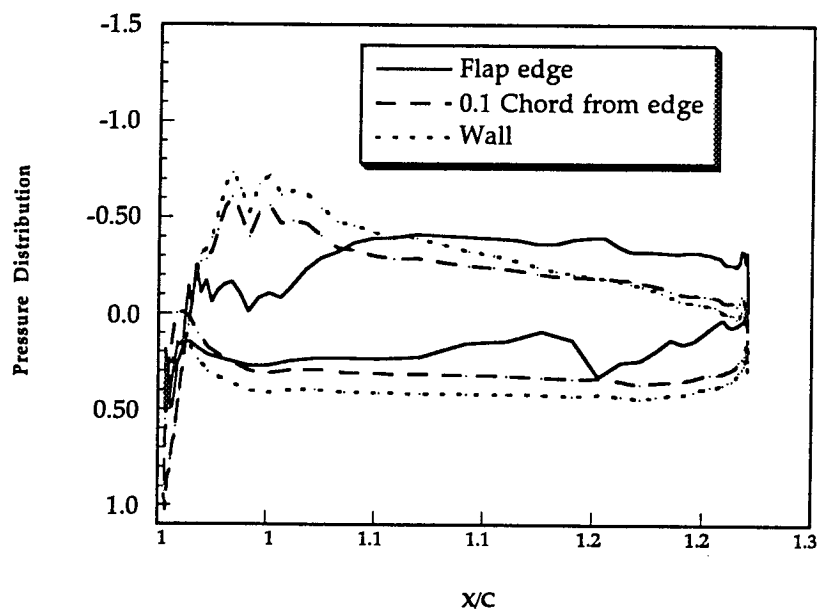


Figure 46: Spanwise pressure variation for landing configuration flap element,  $\alpha = 10^\circ$ .

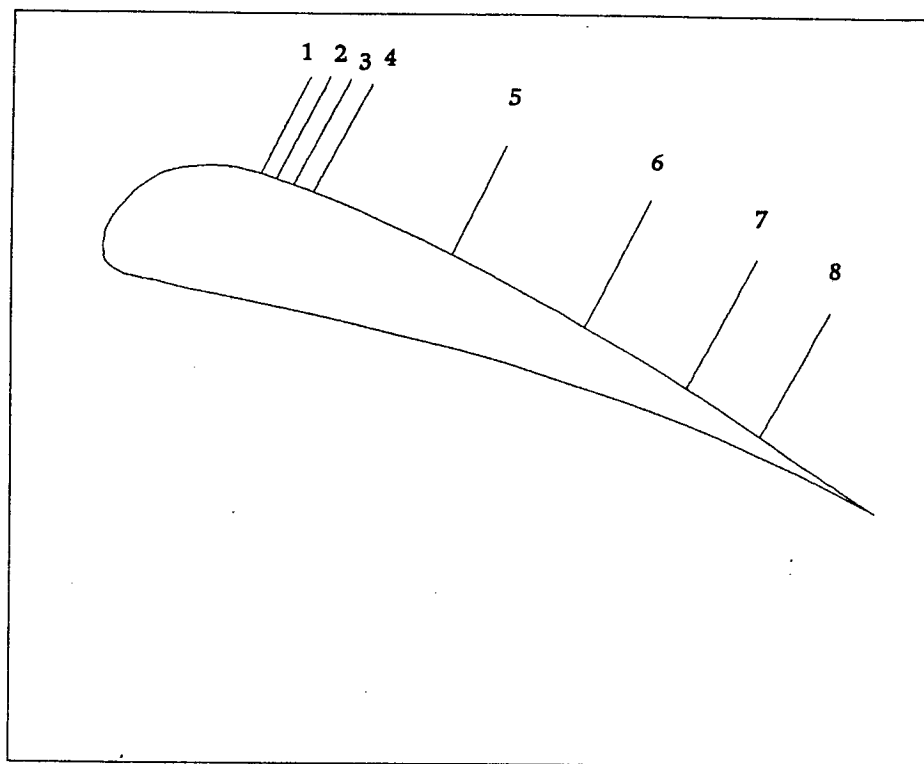


Figure 47: Flap station numbering.

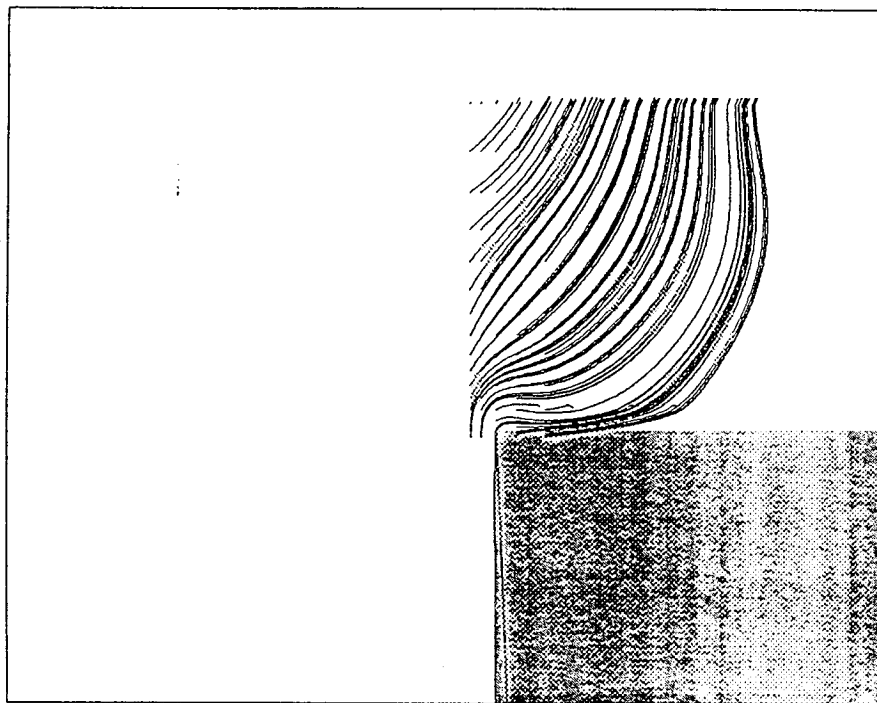


Figure 48: Particle traces at station 1 on flap element in landing position.

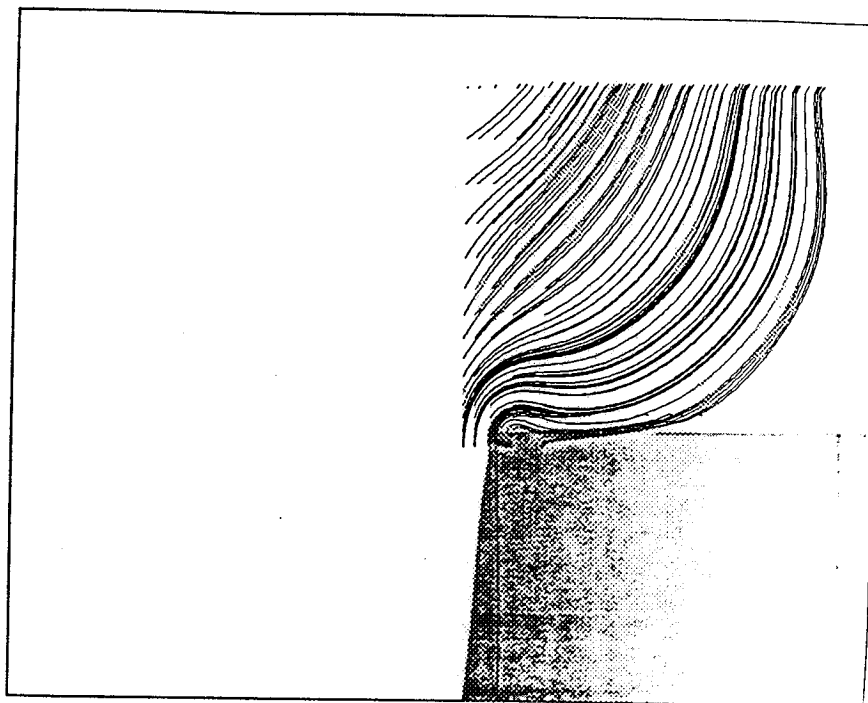


Figure 49: Particle traces at station 2 on flap element in landing position.

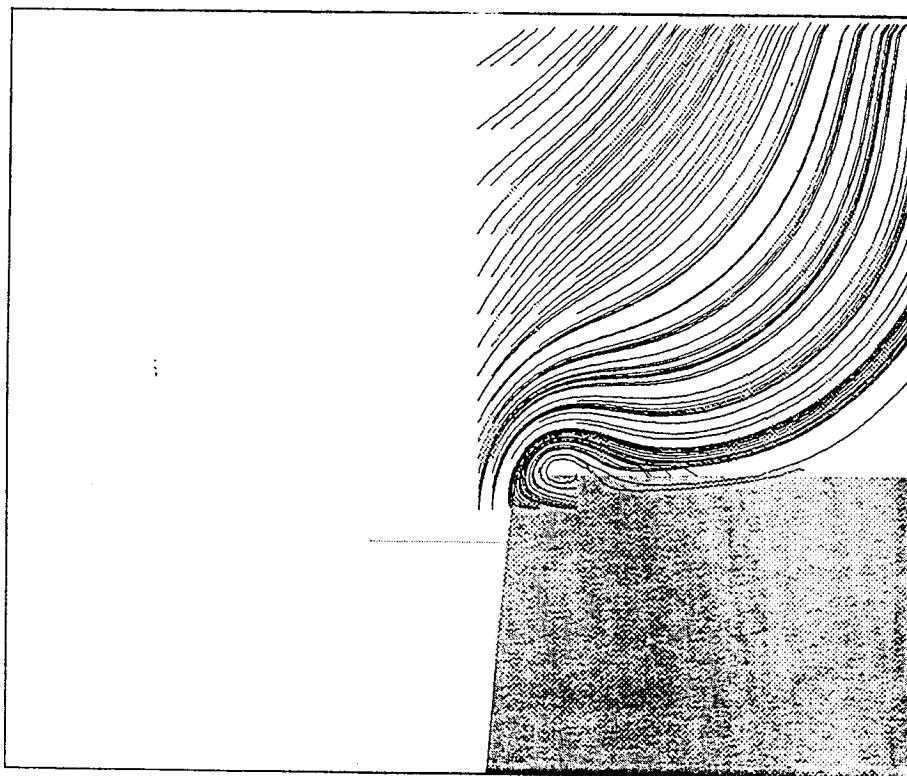


Figure 50: Particle traces at station 3 on flap element in landing position.

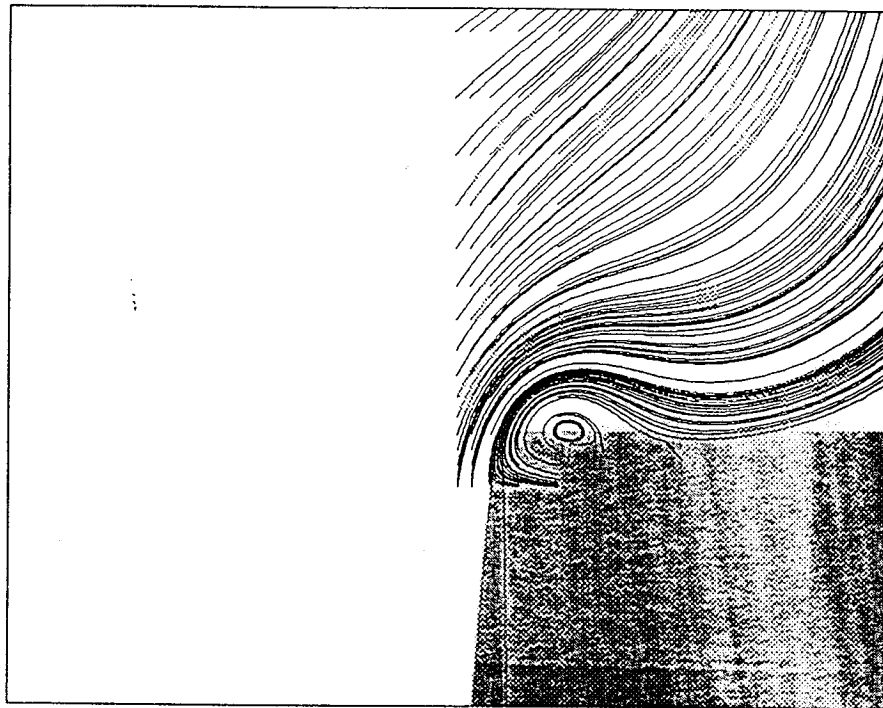


Figure 51: Particle traces at station 4 on flap element in landing position.

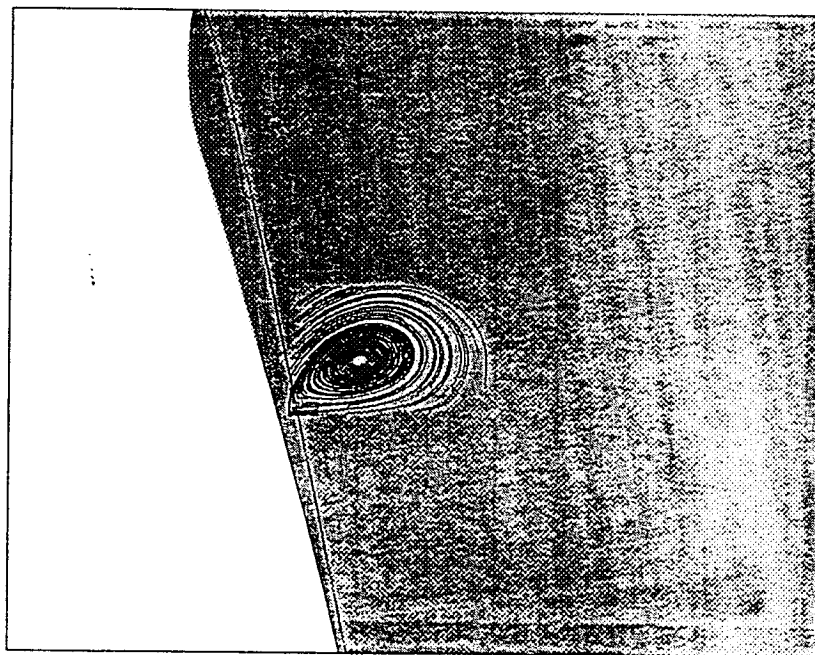


Figure 52: Particle traces at station 5 on flap element in landing position.

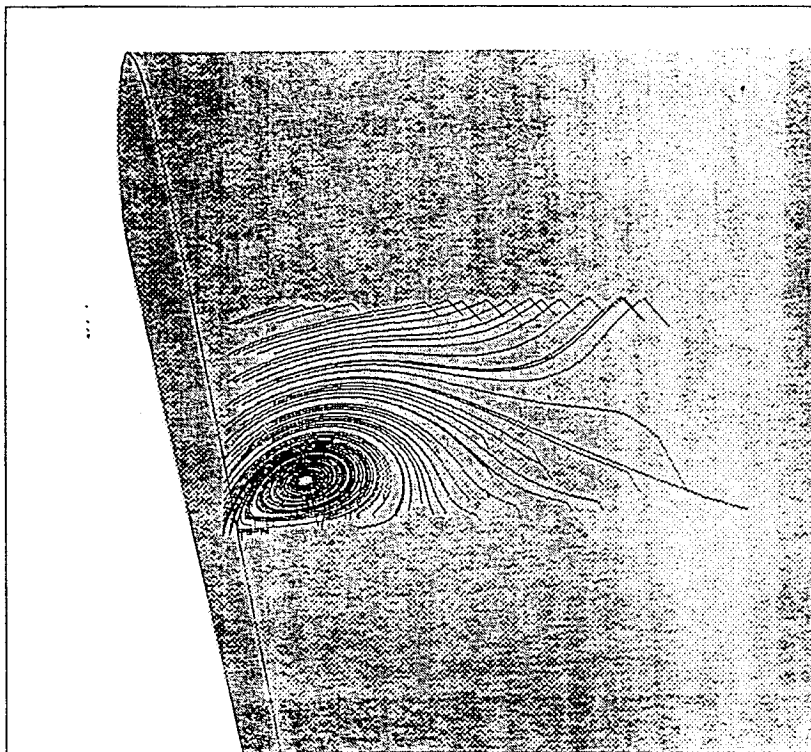


Figure 53: Particle traces at station 6 on flap element in landing position.

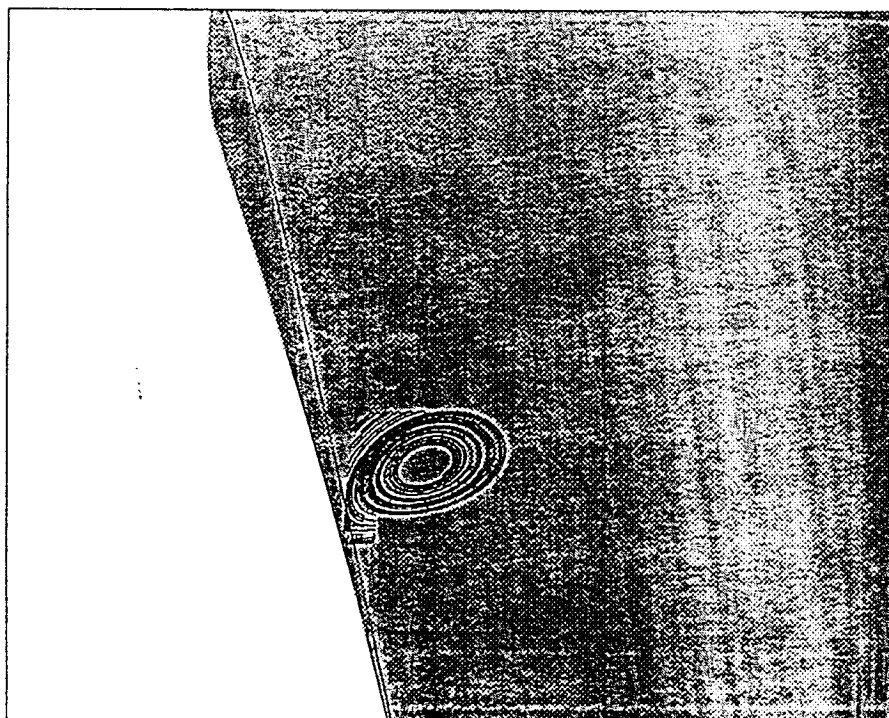


Figure 54: Particle traces at station 7 on flap element in landing position.

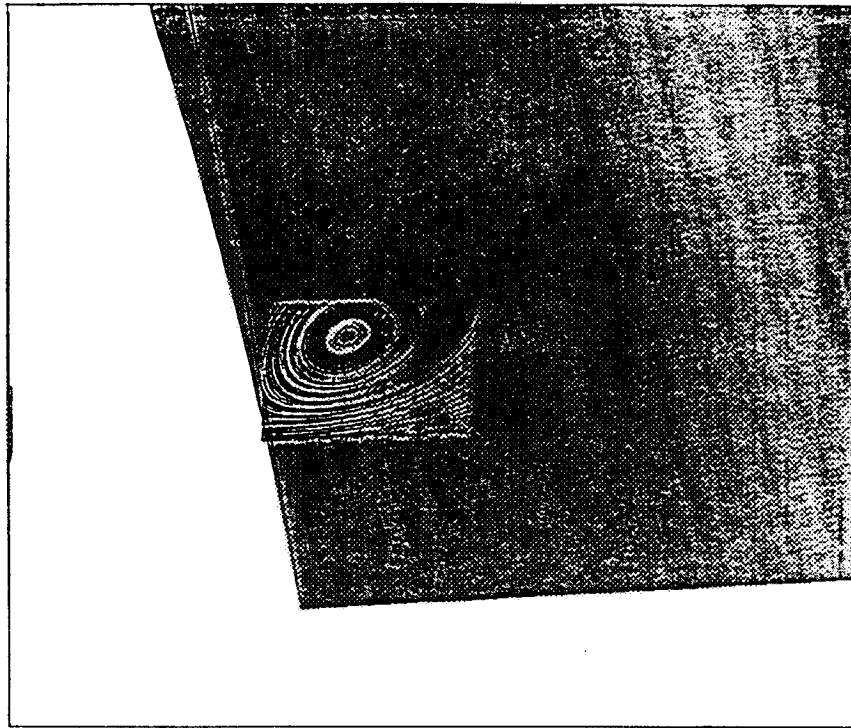


Figure 55: Particle traces at station 8 on flap element in landing position.

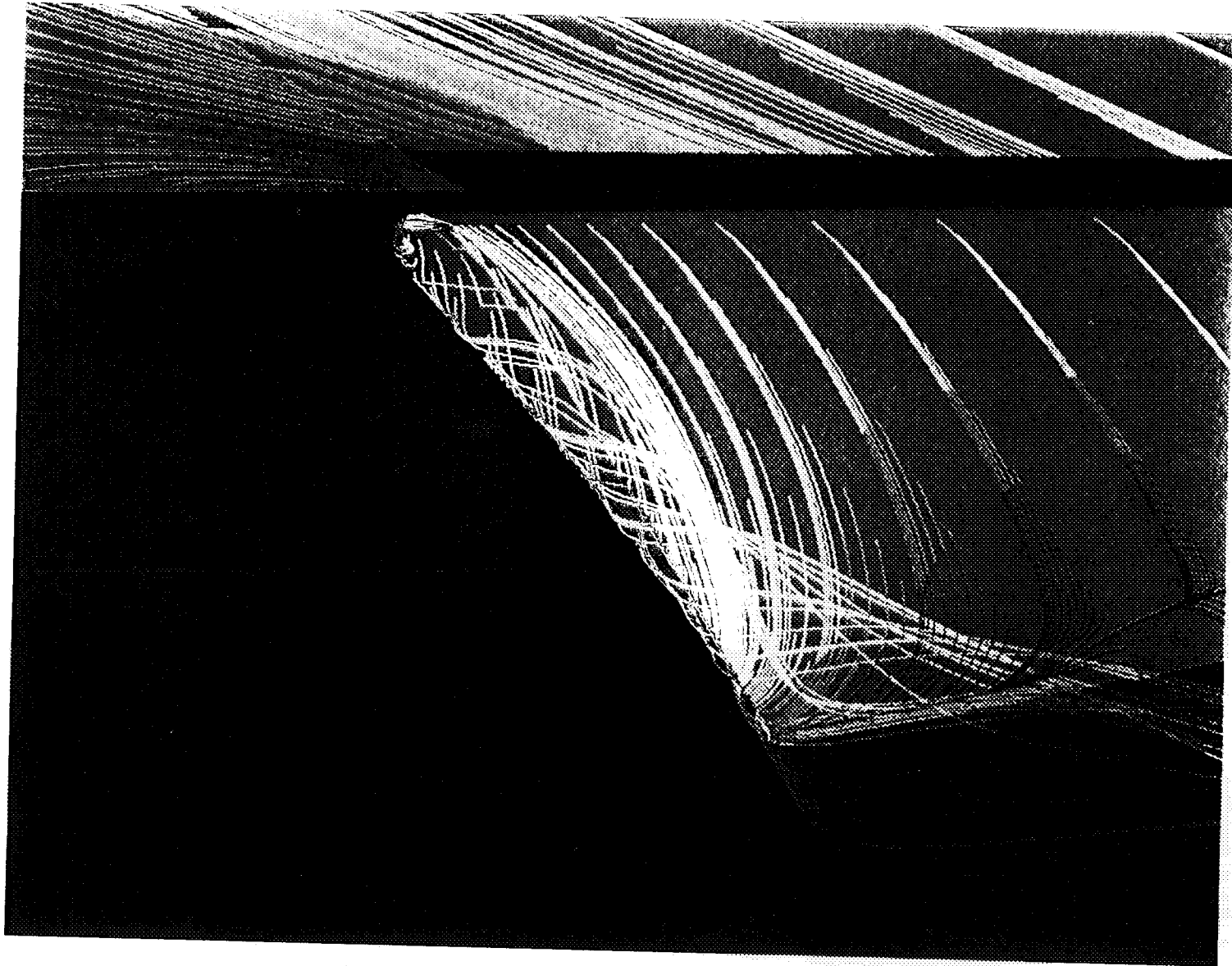


Figure 56: Particle traces colored by pressure at the flap edge of landing configuration.

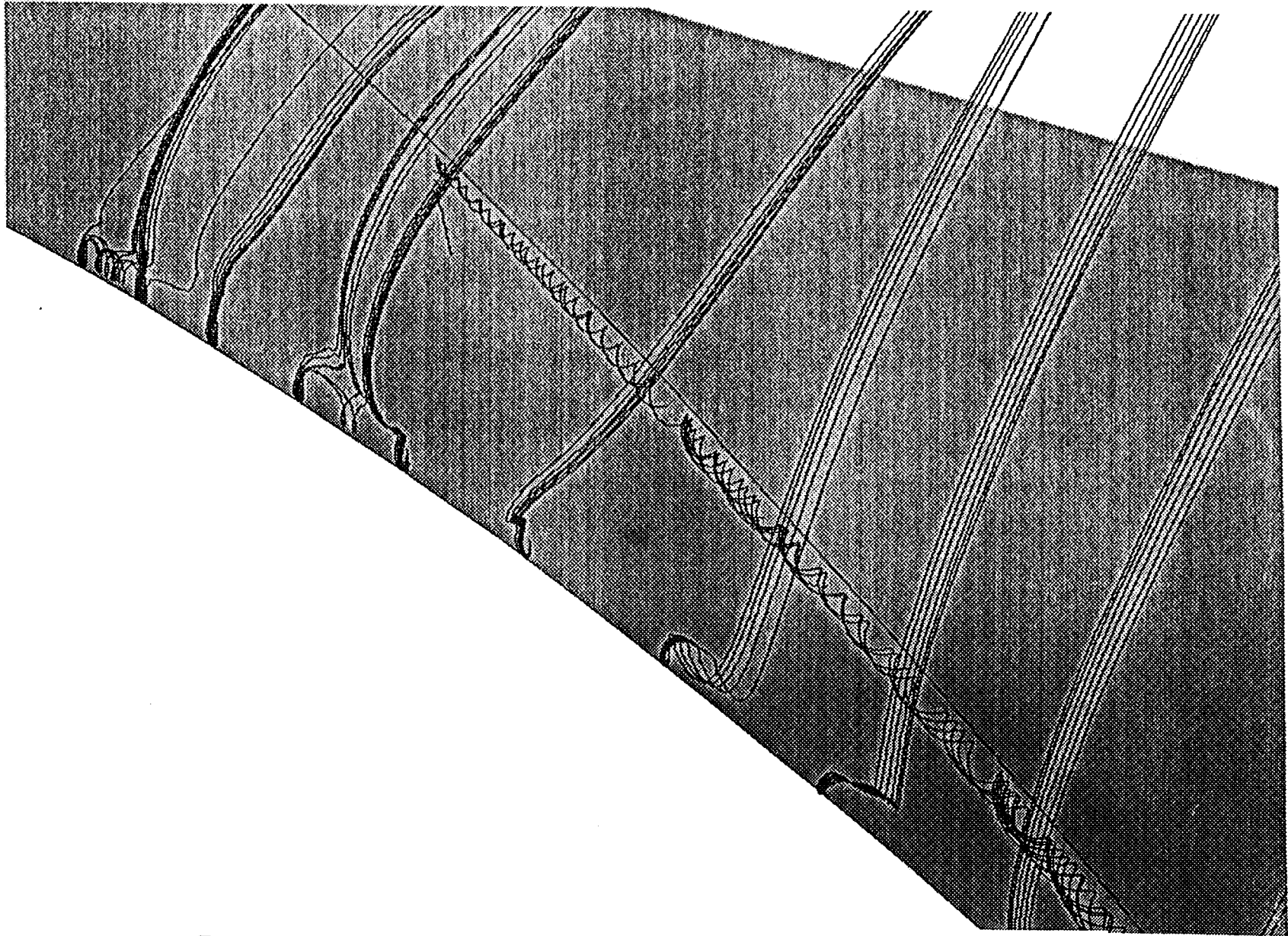


Figure 57: Secondary recirculation regions on flap edge for landing configuration.